On the Mesoscale Structure of Coronal Mass Ejections at Mercury's Orbit: BepiColombo and Parker Solar Probe Observations

Erika Palmerio[1] , Fernando Carcaboso[2] , Leng Ying Khoo[3] , Tarik M. Salman[4,5] , Beatriz Sánchez-Cano[6] ,
Benjamin J. Lynch[7,8] , Yeimy J. Rivera[9] , Sanchita Pal[2] , Teresa Nieves-Chinchilla[4] , Andreas J. Weiss[2] , David Lario[4] ,
Johannes Z. D. Mieth[10] , Daniel Heyner[10] , Michael L. Stevens[9] , Orlando M. Romeo[7,11] , Andrei N. Zhukov[12,13] ,
Luciano Rodriguez[12] , Christina O. Lee[7] , Christina M. S. Cohen[14] , Laura Rodríguez-García[15,16] , Phyllis L. Whittlesey[7] ,
Nina Dresing[17] , Philipp Oleynik[17] , Immanuel C. Jebaraj[17] , David Fischer[18] , Daniel Schmid[18] , Ingo Richter[10] ,
Hans-Ulrich Auster[10] , Federico Fraschetti[9,19] , and Marilena Mierla[12,20]

[1] Predictive Science Inc., San Diego, CA 92121, USA; epalmerio@predsci.com
[2] Postdoctoral Program Fellow, NASA Goddard Space Flight Center, Greenbelt, MD 20771, USA
[3] Department of Astrophysical Sciences, Princeton University, Princeton, NJ 08544, USA
[4] Heliophysics Science Division, NASA Goddard Space Flight Center, Greenbelt, MD 20771, USA
[5] Department of Physics and Astronomy, George Mason University, Fairfax, VA 22030, USA
[6] School of Physics and Astronomy, University of Leicester, LE1 7RH Leicester, UK
[7] Space Sciences Laboratory, University of California, Berkeley, CA 94720, USA
[8] Department of Earth, Planetary, and Space Sciences, University of California, Los Angeles, CA 90095, USA
[9] Center for Astrophysics, Harvard & Smithsonian, Cambridge, MA 02138, USA
[10] Institut für Geophysik und extraterrestrische Physik, TU Braunschweig, D-38106 Braunschweig, Germany
[11] Department of Earth and Planetary Science, University of California, Berkeley, CA 94720, USA
[12] Solar–Terrestrial Centre of Excellence—SIDC, Royal Observatory of Belgium, B-1180 Brussels, Belgium
[13] Skobeltsyn Institute of Nuclear Physics, Moscow State University, 119991 Moscow, Russia
[14] California Institute of Technology, Pasadena, CA 91125, USA
[15] European Space Astronomy Centre, European Space Agency, E-28692 Villanueva de la Cañada, Madrid, Spain
[16] Universidad de Alcalá, Space Research Group (SRG-UAH), E-28801 Alcalá de Henares, Madrid, Spain
[17] Department of Physics and Astronomy, University of Turku, FI-20014 Turku, Finland
[18] Space Research Institute, Austrian Academy of Sciences, A-8042 Graz, Austria
[19] Department of Planetary Sciences, Lunar and Planetary Lab, Tucson, AZ 85721, USA
[20] Institute of Geodynamics of the Romanian Academy, 020032 Bucharest-37, Romania

Abstract

On 2022 February 15, an impressive filament eruption was observed off the solar eastern limb from three remote-sensing viewpoints, namely, Earth, STEREO-A, and Solar Orbiter. In addition to representing the most-distant observed filament at extreme ultraviolet wavelengths—captured by Solar Orbiter's field of view extending to above $6 R_\odot$—this event was also associated with the release of a fast ($\sim$2200 km s^{-1}) coronal mass ejection (CME) that was directed toward BepiColombo and Parker Solar Probe. These two probes were separated by 2° in latitude, 4° in longitude, and 0.03 au in radial distance around the time of the CME-driven shock arrival in situ. The relative proximity of the two probes to each other and the Sun ($\sim$0.35 au) allows us to study the mesoscale structure of CMEs at Mercury's orbit for the first time. We analyze similarities and differences in the main CME-related structures measured at the two locations, namely, the interplanetary shock, the sheath region, and the magnetic ejecta. We find that, despite the separation between the two spacecraft being well within the typical uncertainties associated with determination of CME geometric parameters from remote-sensing observations, the two sets of in situ measurements display some profound differences that make understanding the overall 3D CME structure particularly challenging. Finally, we discuss our findings within the context of space weather at Mercury's distance and in terms of the need to investigate solar transients via spacecraft constellations with small separations, which has been gaining significant attention during recent years.

1. Introduction

Coronal mass ejections (CMEs) can be enumerated among the most spectacular and energetic events in the solar system, consisting of enormous clouds of plasma and magnetic fields that are frequently launched from the Sun into the heliosphere. As they travel (and expand) through the solar corona and interplanetary space, CMEs can experience a myriad of processes, including deflection (e.g., Wang et al. 2004; Liewer et al. 2015; Cécere et al. 2020), rotation (e.g., Yurchyshyn et al. 2007; Vourlidas et al. 2011; Thompson et al. 2012), erosion (e.g., Dasso et al. 2007; Ruffenach et al. 2012; Pal et al. 2021), and deformation (e.g., Savani et al. 2010; Barnard et al. 2017; Braga et al. 2022), due to, e.g., interaction with the structured solar wind (e.g., Isavnin et al. 2013; Heinemann et al. 2019; Davies et al. 2021; Maunder et al. 2022) or other CMEs (e.g., Lugaz et al. 2012; Lugaz & Farrugia 2014; Temmer et al. 2014; Kilpua et al. 2019b). By the time they reach 1 au, CMEs

measure, on average, ~0.3 au in radial size (e.g., Jian et al. 2018) and may have lost their coherence as magnetohydro-dynamic structures (e.g., Owens et al. 2017). The plethora of phenomena that can act on a CME as it journeys away from the Sun may result in structures encountered in situ that are especially difficult to interpret, and even properties such as geoeffectiveness can be altered significantly during propagation due to these evolutionary processes (e.g., Lavraud et al. 2014; Möstl et al. 2015; Liu et al. 2018; Scolini et al. 2020; Winslow et al. 2021; Palmerio et al. 2022b).

Indeed, determination of the global 3D structure of CMEs from in situ measurements, each representing a single 1D trajectory through a humongous plasma cloud, is not a trivial task even in the case of "simpler" situations in which a CME is propagating more or less radially and self-similarly. In this context, multipoint measurements can provide extra constraints on the local structure of a CME at different points throughout its angular extent. The power of multispacecraft observations of CMEs in situ has been known for several decades (e.g., Burlaga et al. 1981), and because of data availability in recent years, multiprobe studies have been gaining increasing attention. However, most multipoint measurements are attained over arbitrary radial and angular separations of the spacecraft involved (e.g., Davies et al. 2022; Möstl et al. 2022; Rodríguez-García et al. 2022), making it particularly difficult to attribute structural and compositional differences of the investigated CMEs to radial evolution, longitudinal (local) variations, or both. Even more so, the difficulties only increase as CMEs are probed beyond 1 au and toward the outer heliosphere, mainly due to heightened chances of interactions and mergers of initially separated structures (e.g., Rodriguez et al. 2008; Witasse et al. 2017; Palmerio et al. 2021). Nevertheless, there are some "special" cases of spacecraft configurations that are of particular interest for CME studies, i.e., those that involve small longitudinal separations, allowing focused analyses of radial evolution (e.g., Good et al. 2019; Vršnak et al. 2019; Salman et al. 2020), or small radial separations, permitting investigations of the overall structure at one snapshot in time (e.g., Kilpua et al. 2009; Farrugia et al. 2011; Lugaz et al. 2022).

An additional "special" case in terms of relative spacecraft configurations takes place when the probes involved are characterized by small longitudinal and radial separations at the same time, thus providing the opportunity to examine the mesoscale structure of CMEs. Such relative arrangements are rarely attained fortuitously, but a few studies have taken advantage of a number of favorable periods featuring pairs of probes that happened to orbit close to each other in near-Earth space. For example, Lugaz et al. (2018) and Ala-Lahti et al. (2020) analyzed variations in the magnetic ejecta (for 21 events) and sheath region (for 29 events) structures, respectively, observed by spacecraft that were separated by ≲0.01 au in absolute distance. Lugaz et al. (2018) found that, in the case of CME ejecta, the magnetic field magnitude has typical scale lengths of longitudinal magnetic coherence of 0.25–0.35 au (corresponding to 14°–20° at 1 au), while the single magnetic components maintain their coherence over scales of 0.06–0.12 au (corresponding to 3°–7° at 1 au). On the other hand, Ala-Lahti et al. (2020) found that, in the case of CME-driven sheaths, the largest scale of coherence is achieved by the east–west component of the magnetic field, with values lying around ~0.15 au (corresponding to ~9° at 1 au), while the
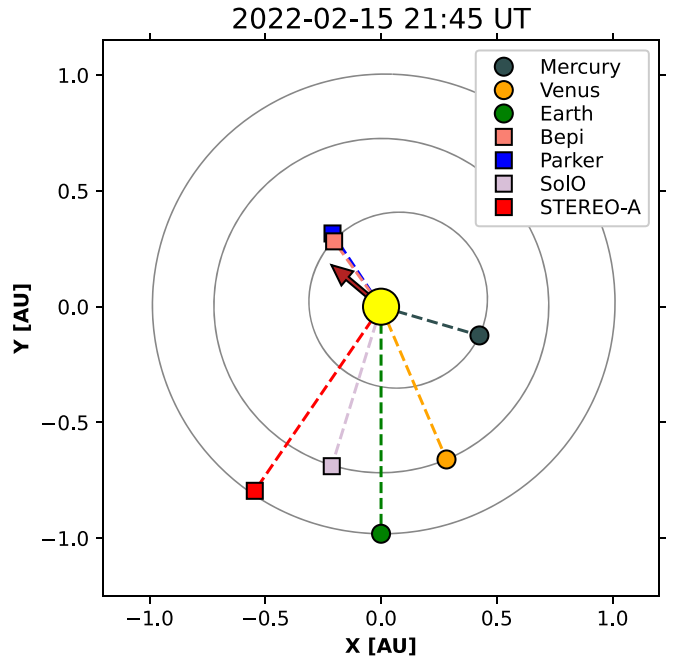

Figure 1. Position of planets and spacecraft within 1 au from the Sun on 2022 February 15 at 21:45 UT, i.e., around the CME eruption time. The propagation direction of the CME inferred from 3D reconstructions of the eruption in the corona is indicated with an arrow. The orbits of Mercury, Venus, and Earth are also shown.

magnetic field magnitude and the remaining components have typical scale lengths of 0.02–0.04 au (corresponding to 1°–2° at 1 au). Other studies that investigated the magnetic configuration of CMEs over relatively short spatial scales at the heliocentric distance of ~1 au include that of Davies et al. (2021), who analyzed a single event and did not report significant differences in the structure observed at two spacecraft separated by ~0.02 au radially and ~1° longitudinally.

It is clear from the studies mentioned above that, in the context of CME research, the mesoscale region of the parameter space—defined by Lugaz et al. (2018) as the critical region characterized by radial separations of 0.005–0.050 au and angular separations of of 1°–12°—is left largely unexplored to this day, especially considering that all investigations to date have been possible only via measurements collected at Earth's orbit. In this work, we analyze in detail the in situ structure of the 2022 February 15 CME. This eruption has already gained attention in the heliophysics community because it represents the most-distant filament observed at extreme-ultraviolet (EUV) wavelengths (Mierla et al. 2022), but the scientific significance of this event goes beyond its exceptional remote-sensing measurements. In fact, the CME associated with this eruption was seen in situ by BepiColombo (Bepi; Benkhoff et al. 2021) and Parker Solar Probe (Parker; Fox et al. 2016), which were relatively close to each other and only ~0.35 au away from the Sun (see Figure 1). Hence, the 2022 February 15 CME represents the first occasion to investigate the mesoscale structure of CMEs at Mercury's orbit. The work presented here consists of a detailed analysis of the shock, sheath region, and magnetic ejecta observed at the two spacecraft and aims to enhance our current understanding of the structure and evolution of CMEs at relatively early stages of their journey through interplanetary space.
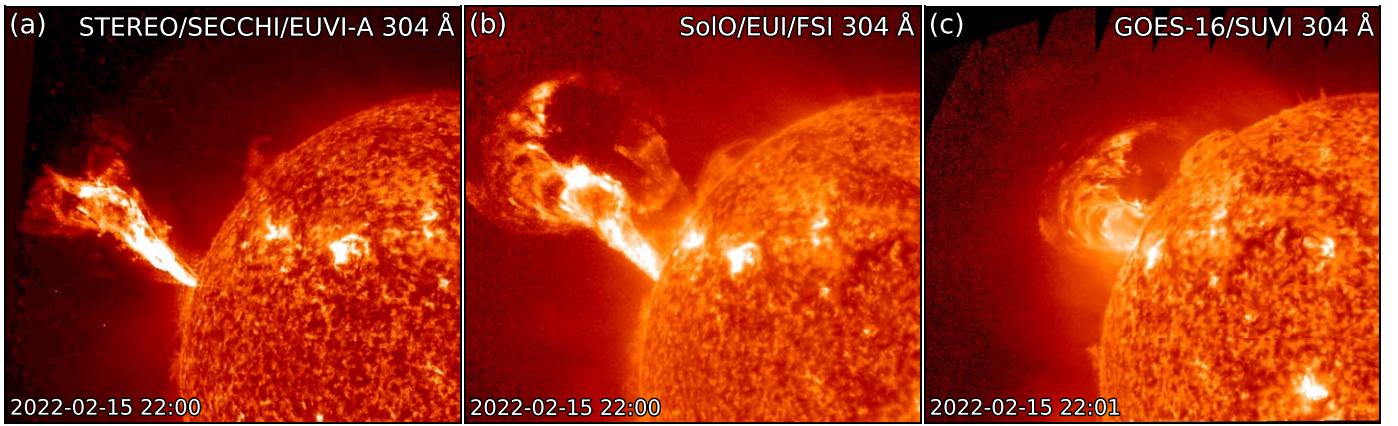
Figure 2. The 2022 February 15 filament eruption at ∼22:00 UT as observed in EUV (304 Å channel) from the available viewpoints. (a) STEREO/SECCHI/EUVI-A data. (b) SolO/EUI/FSI data. (c) GOES-16/SUVI data, representing Earth's view. In all images, the off-limb emission has been enhanced with a radial filter.

2. Overview of the 2022 February 15 Eruption

In this section, we provide a brief overview of the remote-sensing observations associated with the 2022 February 15 eruption in both the EUV and white-light (WL) regimes. For an in-depth discussion of the various substructures that can be identified in the available multispacecraft imagery, we direct the reader to Mierla et al. (2022).

2.1. EUV Observations

As mentioned in the Introduction, a large filament was involved in the 2022 February 15 eruption. The event was observed at EUV wavelengths from three viewpoints (see Figure 1 for their positions), namely, the Solar Terrestrial Relations Observatory Ahead (STEREO-A; Kaiser et al. 2008) and Solar Orbiter (SolO; Müller et al. 2020) spacecraft, as well as near Earth—in this work, we use imagery from the Geostationary Operational Environmental Satellites 16 (GOES-16) probe. An overview of the remote-sensing EUV observations of the erupting filament from these three locations is shown in Figure 2, displaying data from the Extreme UltraViolet Imager (EUVI) telescope, part of the Sun Earth Connection Coronal and Heliospheric Investigation (SECCHI; Howard et al. 2008) suite on board STEREO-A; the Full Sun Imager (FSI) telescope, part of the Extreme Ultraviolet Imager (EUI; Rochus et al. 2020) suite on board SolO; and the Solar UltraViolet Imager (SUVI; Darnel et al. 2022) telescope on board GOES-16. From these observations, it is clear that the 2022 February 15 eruption appeared as a behind-the-eastern-limb event from all three viewpoints, albeit to different extents. If we consider the average of the spatial range spanned by various filament and CME features in 3D as triangulated by Mierla et al. (2022), i.e., E138N35 in Stonyhurst coordinates, then the event took place behind the eastern limb by ∼15° for STEREO-A, ∼30° for SolO, and ∼50° for Earth.

The erupting filament was first observed to emerge from behind the northeastern limb from all three viewpoints around 21:50 UT on 2022 February 15. Its fine structure was best visible at 304 Å (i.e., the channel shown in Figure 2), but its appearance was also prominent at 171 Å from all three imagers, in addition to being observed at several other EUV wavelengths (depending on the availability of each instrument). During the early phases of the eruption, the filament appeared to be surrounded by a "bubble-like" leading edge (see Figures 2

and 5 in Mierla et al. 2022), the resulting structure being reminiscent of the classic three-part CME that is usually observed in coronagraph data (e.g., Illing & Hundhausen 1985; Vourlidas et al. 2013). Throughout its evolution across the fields of view of the three different telescopes (we note that the SolO/EUI/FSI field extended up to $>6\,R_\odot$ at the time of this event; see Mierla et al. 2022), the filament propagated in a northeasterly direction, away from the solar equatorial plane. This suggests that any near-the-ecliptic probe detecting this CME in situ would likely experience a flank encounter rather than a central one, assuming that no dramatic equatorward deflections would take place in the outer corona and/or interplanetary space (since stronger CMEs tend to be less affected by the configuration of the coronal and interplanetary magnetic field; e.g., Gui et al. 2011; Kay et al. 2015).

2.2. WL Observations

The 2022 February 15 eruption was observed in WL imagery from two viewpoints, i.e., the STEREO-A spacecraft and Earth—although SolO is equipped with a coronagraph, the instrument was not operational at the time of this event. From the STEREO-A viewpoint, the apex of the CME first appeared around 21:55 UT in the COR1 field of view and around 22:10 UT in the COR2 one, both cameras being part of the SECCHI suite. From Earth's viewpoint, the CME was observed by the Large Angle Spectroscopic Coronagraph (LASCO; Brueckner et al. 1995) on board the Solar and Heliospheric Observatory (SOHO; Domingo et al. 1995), emerging around 22:10 UT in the C2 field of view and around 22:30 UT in the C3 one. An overview of the remote-sensing WL observations of the CME in the solar corona from these two locations is shown in Figure 3.

From coronagraph data, it is evident that the 2022 February 15 CME displayed clear shock signatures, usually manifested as a fainter emission that surrounds the brighter magnetic ejecta (e.g., Vourlidas et al. 2003; Kouloumvakos et al. 2022). Additionally, the CME propagated toward the northeast from both available viewpoints, in agreement with the EUV observations presented in Section 2.1. To obtain a more quantitative estimate of the CME geometric and kinematic parameters, we fit the Graduated Cylindrical Shell (GCS; Thernisien 2011) model to WL data. The GCS model consists of a parameterized shell (described by six variables) that can be projected onto nearly simultaneous coronagraph images from different perspectives and is then manually adjusted to best
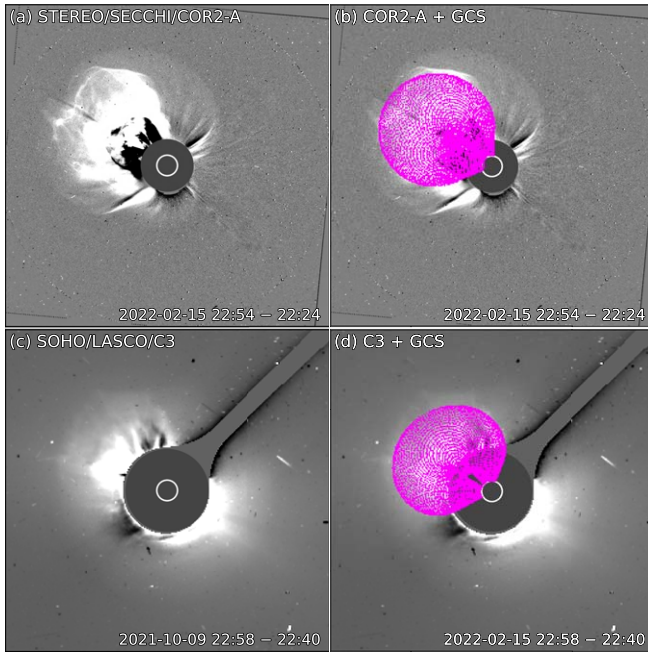
Figure 3. The 2022 February 15 CME at ∼23:00 UT as observed in WL (coronagraph) difference imagery from the available viewpoints. (a) STEREO/ SECCHI/COR2-A data, shown also in (b) with the GCS wireframe overlaid. (c) SOHO/LASCO/C3 data, shown also in (d) with the GCS wireframe overlaid.

Table 1
Times and Positions of Bepi and Parker When Crossing CME-related Features

CME Feature	Time [UT]	Position $[r, \theta, \phi]$
Bepi		
Shock	2022-02-16T06:25	[0.35, 1.71, −142.73]
Ejecta start	2022-02-16T15:41	[0.34, 1.78, −140.99]
Ejecta end	2022-02-17T07:51	[0.34, 1.91, −137.89]
Parker		
Shock	2022-02-16T07:25	[0.37, 3.71, −145.92]
Cloud start	2022-02-16T15:18	[0.36, 3.70, −145.43]
Cloud end	2022-02-17T06:32	[0.35, 3.67, −144.39]
Obstacle end	2022-02-17T16:48	[0.33, 3.64, −143.58]

Note. The $[r, \theta, \phi]$ triplets are reported in Stonyhurst coordinates in units of [au, deg, deg]. See the text throughout Section 3 for a discussion of the identification of all the boundaries.

3. In Situ Observations at Bepi and Parker

In this section, we provide an overview of the available in situ measurements of the 2022 February 15 CME at Bepi and Parker. We first show a comparison of the magnetic field data at both spacecraft, followed by a more detailed summary of magnetic field and plasma observations at Parker; the plasma instruments on board Bepi are not regularly operational during cruise phase (i.e., preceding the Mercury orbit insertion scheduled for 2025 December). Additionally, we remark that the magnetic field data from Bepi have been subject to additional processing due to the spacecraft's solar electric propulsion system (SEPS) being activated during the period of interest (more information is provided in Appendix B). The timings of the various CME-related features discussed in the following sections, together with the exact positions of Bepi and Parker when crossing each, are summarized in Table 1.

3.1. Magnetic Field Measurements at the Two Spacecraft

Given the high speed of the 2022 February 15 CME as inferred from remote-sensing observations (see Section 2.2), we can expect a relatively rapid propagation to ∼0.35 au, i.e., the heliocentric distance of Bepi and Parker at the time of the event (see Figure 1). The two probes were located ∼15° to the east and ∼30° to the south of the CME nose trajectory that was estimated from GCS fitting. By inspecting magnetic field measurements from the Mercury Planetary Orbiter Magnetometer (MPO-MAG; Heyner et al. 2021) on board Bepi and the Fluxgate Magnetometer part of the FIELDS (Bale et al. 2016) investigation on board Parker—both data sets are shown in Figure 4—we find signatures of a solar wind transient starting on February 16 around 07:00 UT (approximate average time between the two spacecraft). This yields a travel time of ∼9.25 hr, with an average transit speed of 1620 km s^{-1}. Specifically, we observe an abrupt increase in the magnetic field magnitude at 06:25 UT in Bepi data and 07:25 UT in Parker data (marked with vertical gray lines in Figure 4), indicating the passage of a CME-driven shock; by considering the exact shock arrival times and positions for each spacecraft, we obtain average transit speeds of 1672 km s^{-1} at Bepi and 1606 km s^{-1} at Parker. The identification of this feature as a fast-forward shock can be confirmed using plasma data from Parker (presented in detail in Section 3.2); hence, it is reasonable to assume that the same holds true for Bepi.

The 2022 February 15 CME is shown in the right panels of Figure 3. According to our results, the CME apex propagates at a latitude of 33° and longitude of −130° (both values are given in Stonyhurst coordinates), the CME axis has a tilt of −60° with respect to the solar equator (defined as positive for counterclockwise rotations from the solar west direction), the CME half-angular width along its major axis is ∼45°, and the CME radial speed in the solar corona is ∼2200 km s^{-1}. These values are in excellent agreement with those reported in Mierla et al. (2022), who estimated a propagation direction of 34° in latitude and −132° in longitude, as well as a speed of ∼2200 km s^{-1}. It is evident from the GCS fitting shown in Figure 3 and our resulting parameters that the 2022 February 15 CME was characterized by a high latitude and inclination. This indicates that a near-the-ecliptic spacecraft encountering the ejecta in situ would likely cross its southern flank, as already speculated when considering EUV observations (see Section 2.1).

After leaving the solar corona, the 2022 February 15 CME was observed in WL heliospheric imagery by the Wide-Field Imager for Solar Probe Plus (WISPR; Vourlidas et al. 2016) suite of cameras on board Parker. Only the southern portion of the full structure was captured in the fields of view of the WISPR telescopes, further proving that the CME continued propagating in interplanetary space with a prominent northward component, and that equatorward deflections are not expected to have taken place. These observations are presented and briefly discussed in Appendix A.
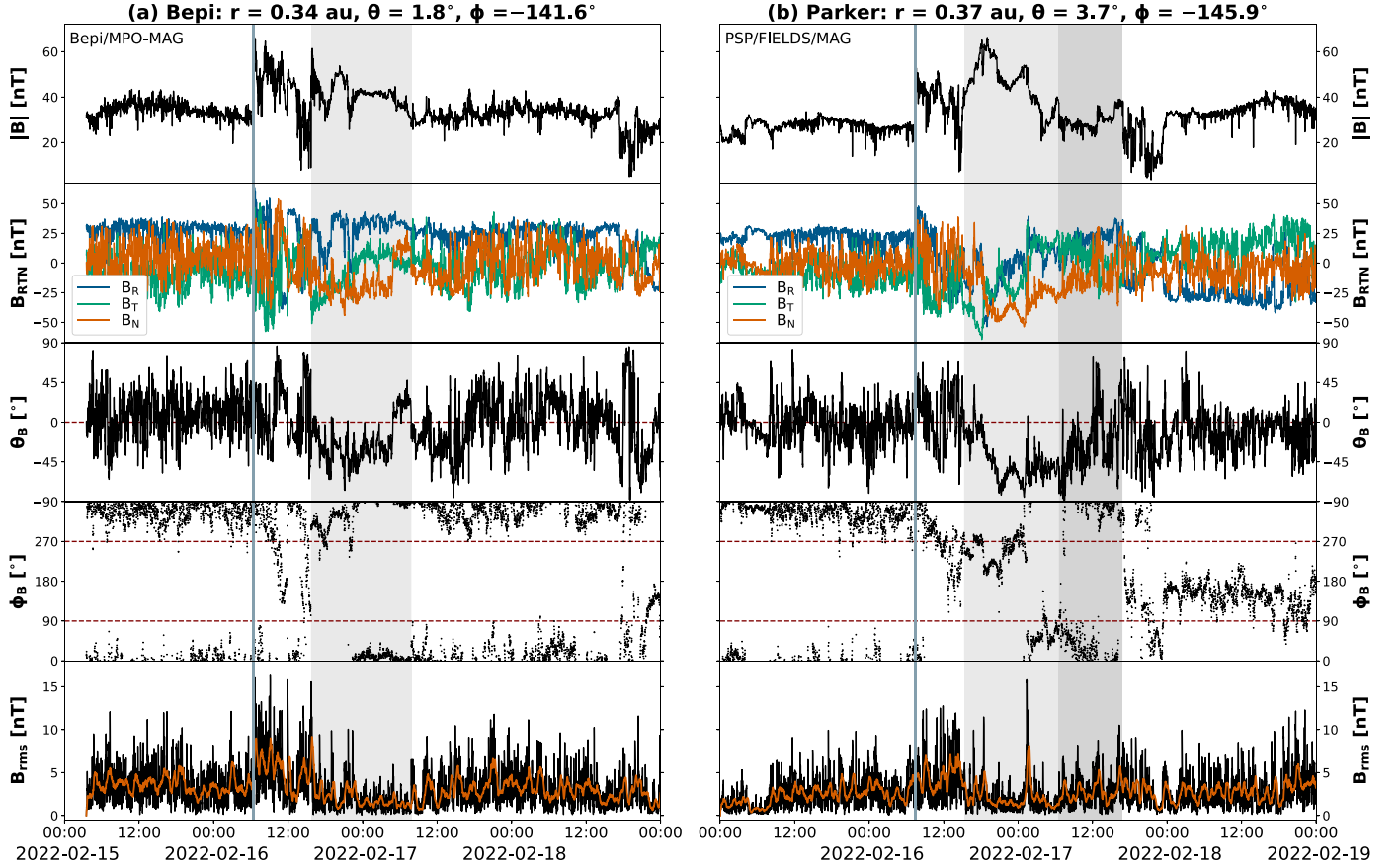
Figure 4. Magnetic field measurements (1 minute cadence) at (a) Bepi and (b) Parker for the period 2022 February 15–18. Each plot shows, from top to bottom: magnetic field magnitude, magnetic field Cartesian components in RTN coordinates, latitudinal angle of the magnetic field, longitudinal angle of the magnetic field, and rms error of the magnetic field (using a rolling average over 15 minutes for each component, the superposed orange curve displays the 30 minute rolling average of the same data). The (r, θ, ϕ) values displayed at the top of the panels for both spacecraft refer to 2022 Feburary 16, 07:00 UT, and the angles are reported in Stonyhurst coordinates. The vertical gray lines indicate the arrival of the CME-driven shock at either spacecraft, while the gray shaded areas highlight the CME ejecta. At Parker, the full ejecta (magnetic obstacle) includes both gray regions, and the flux rope (magnetic cloud) structure within it is represented by the lighter gray area. Additional details about the identification of boundaries at Parker are provided in Section 3.2.

After a period (∼8.5 hr) characterized by highly fluctuating magnetic field vectors corresponding to the turbulent sheath region that usually follows CME-driven shocks, around 15:30 UT (approximate average time between the two spacecraft), both probes observed enhanced magnetic field magnitudes, together with smoother profiles of the field components, which can be attributed to the passage of the CME ejecta (highlighted as gray shaded areas in Figure 4). This corresponds to a travel time of ∼17.67 hr, with an average transit speed of 823 km s^{-1}. Specifically, the leading edge of this structure is identified on February 16 at 15:41 UT for Bepi and 15:18 UT for Parker, resulting in average ejecta transit speeds of 798 and 861 km s^{-1}, respectively. We note that Parker observed the ejecta leading edge slightly earlier despite being ∼0.02 au farther from the Sun than Bepi at the time (see Table 1). This suggests that Parker may have been somewhat closer to the CME nose given its higher heliocentric latitude and the CME propagation direction being mainly above the ecliptic, or that the probes encountered a highly distorted CME front. At both spacecraft, the magnetic field vectors rotated smoothly from east to west and pointed mostly southward throughout the structure, suggesting approximately an east–southwest (right-handed) flux rope type from visual inspection (e.g., Bothmer & Schwenn 1998; Palmerio et al. 2018). While at Bepi, the entire identified CME ejecta interval was

characterized by flux-rope-like signatures, at Parker, the trailing portion of the structure featured more turbulent magnetic fields (especially in the north–south component), suggesting that the flux rope and, more generally, the ejecta boundaries may not coincide (e.g. Richardson & Cane 2010; Kilpua et al. 2013; more details on this matter are provided in Section 3.2). For simplicity and to avoid confusion, we shall refer henceforth to the flux rope interval as the "magnetic cloud" (e.g., Burlaga et al. 1981) and to the whole CME ejecta as the "magnetic obstacle" (e.g., Nieves-Chinchilla et al. 2019).

We also investigate the level of fluctuation in the interplanetary magnetic field by computing the rms of the field vector, shown in Figure 4, using

$$B_{\rm rms} = \sqrt{\sum_{i=R,T,N} \frac{(B_i - \langle B_i \rangle)^2}{n}}, \qquad (1)$$

where for the averaged quantities we employ 15 minute rolling averages of the corresponding magnetic field component and n is the number of data points employed for each average (hence, $n = 15$ here). It is evident that the portion of solar wind identified as the sheath region in either data set generally features the most fluctuations when compared to the ambient medium and the CME ejecta material, in agreement with

statistical studies of interplanetary CMEs detected at 1 au (e.g., Masías-Meza et al. 2016; Kilpua et al. 2019a). At Bepi, the level of fluctuation displays a rather clear decrease inside the magnetic ejecta with respect to the entire time series, as expected from statistical studies of CMEs measured at 1 au (e.g., Rodriguez et al. 2016; Regnault et al. 2020). At Parker, the same holds generally true, but we note that the largest fluctuations of the entire time series are reached briefly in the middle of the ejecta due to a sudden change in the magnetic field vector. Additionally, we observe a relatively higher level of fluctuations in the second part of the ejecta (i.e., outside of the magnetic cloud interval), which is to be expected since flux rope ejecta tend to display more organized magnetic fields (e.g., Li et al. 2018; Nieves-Chinchilla et al. 2019).

3.2. Magnetic Field and Plasma Measurements at Parker

As mentioned at the beginning of this section, the available in situ observations at Parker for the 2022 February 15 event include plasma data, which, on the other hand, do not find a direct comparison at Bepi due to the corresponding instrument (s) not being operational. The whole set of in situ observations at Parker is presented in Figure 5, where the FIELDS magnetic field data are complemented with plasma measurements from the Solar Wind Electrons Alphas and Protons (Kasper et al. 2016) suite—specifically, using the Solar Probe Cup (SPC; Case et al. 2020), Solar Probe ANalyzer-Ions (SPAN-i; Livi et al. 2022), and Solar Probe ANalyzer-Electrons (SPAN-e; Whittlesey et al. 2020) detectors. Here, we use the collective of these observations to better constrain and define the various CME features and substructures that were briefly introduced in Section 3.1. We note that there is a data gap in the SPC proton moments immediately following the detection of the CME-driven shock due to the solar wind being outside of the instrument's energy range (bulk speed $\gtrsim 800 \, \mathrm{km \, s^{-1}}$). SPAN-i data, on the other hand, despite capturing the profile of the solar wind speed in its entirety, considerably underestimate the proton density and temperature due to the full ion distribution not being in the instrument's field of view. Hence, we complement the available proton density and temperature measurements from SPC with electron data from SPAN-e derived from fitting to the electron core distribution (using the procedure described in Romeo et al. 2023).

First of all, we note that the abrupt magnetic field jump that we had identified as the CME-driven shock in Section 3.1 (vertical gray line in Figure 5) is indeed accompanied by a prominent rise in the solar wind bulk speed (from ~ 550 to $\sim 850 \, \mathrm{km \, s^{-1}}$), a moderate climb in the electron density and temperature, as well as an intensification of suprathermal electron fluxes (the electron flux enhancements observed prior to the shock arrival are due to the strong particle event associated with this eruption analyzed by, e.g., Giacalone et al. 2023; Khoo et al. 2024). The following sheath region is characterized by highly fluctuating magnetic fields, almost-constant speeds, a declining temperature profile, and a plateauing density trend except for a high-density feature close to its trailing portion. The density peak at the back of the sheath is reminiscent of a piled-up compression (PUC) region that forms ahead of the nose of a driver (in this case, the CME ejecta), often due to its large expansion speed, which is known to usually be higher close to the Sun and then to decrease

gradually as the CME travels through interplanetary space (e.g., Farrugia et al. 2008; Das et al. 2011).

Regarding the CME ejecta (gray shaded area in Figure 5), we use the plasma measurements to corroborate our initial assessment of noncoinciding magnetic cloud and magnetic obstacle boundaries (see Section 3.1). Indeed, we note that bidirectional suprathermal electrons—i.e., with a pitch angle distribution (PAD) displaying peaks close to $0°$ and $180°$—are detected throughout the identified CME ejecta interval. This feature is usually interpreted as the result of two electron beams flowing along and against the magnetic field lines and is often associated with closed lines that are connected to the Sun from both ends, especially in the case of CME ejecta (e.g., Gosling et al. 1987; Carcaboso et al. 2020). Additionally, we find that the magnetic cloud period (characterized by smoother and rotating magnetic fields) features a declining speed profile, usually interpreted as a signature of expansion (e.g., Zurbuchen & Richardson 2006; Nieves-Chinchilla et al. 2018b). The trailing portion of the magnetic obstacle (where magnetic fluctuations are higher), on the other hand, displays first a plateauing and then a slightly rising speed trend, suggesting that expansion of the structure had likely ceased in that region and was possibly related to the small rise in magnetic field magnitude over the last $\sim 5 \, \mathrm{hr}$ of the ejecta passage. The temperature and plasma beta show rather irregular profiles, but they display periods with values below the ambient ones throughout the ejecta interval. The density is generally never below ambient values and features an isolated peak inside the magnetic cloud interval (coinciding with a local maximum in the electron temperature as well). A possible cause for the observed mismatching magnetic cloud and magnetic obstacle boundaries is flux erosion (more details on this aspect are presented in Section 4.3).

From the He/H composition panel, we note that the He abundances rise throughout the sheath toward the ejecta (gray region in Figure 5). Prior to the shock, the solar wind He/H abundance appears below 1%, which is typical of solar wind values (e.g., Borrini et al. 1981). The gradual rise in the He/H values throughout the sheath indicates there is no sharp boundary between the solar wind, the sheath/shocked plasma, and the main CME ejecta. The smooth transition is consistent with a gradual accumulation and mixture of solar wind and CME material in the front. Moreover, there are also some He/H enhancements that appear throughout the trailing part of the ejecta, which is in qualitative agreement with the Rodriguez et al. (2016) superposed epoch profile obtained from 1 au events and may result from He gravitational settling in the preeruption CME source region (e.g., Richardson & Cane 2004). The fluctuations in the He abundance could indicate the passage of coherent substructure in connection to the filament's fragmented nature observed in the remote-sensing images (see Section 2.1). However, due to the field-of-view restrictions of SPAN-i, many of the measurements are omitted across this time frame, making it difficult to examine with certainty. Previous work has shown that He/H abundances are generally elevated in CMEs compared to the solar wind (Borrini et al. 1982; Zurbuchen et al. 2016). However, it remains unclear whether filaments themselves contain high He/H abundances (Lepri & Rivera 2021; Rivera et al. 2022). For a similarly energetic CME, the Bastille Day CME that erupted on 2000 July 14 and reached $2000 \, \mathrm{km \, s^{-1}}$ in the low corona, its compositional structure indicated that the
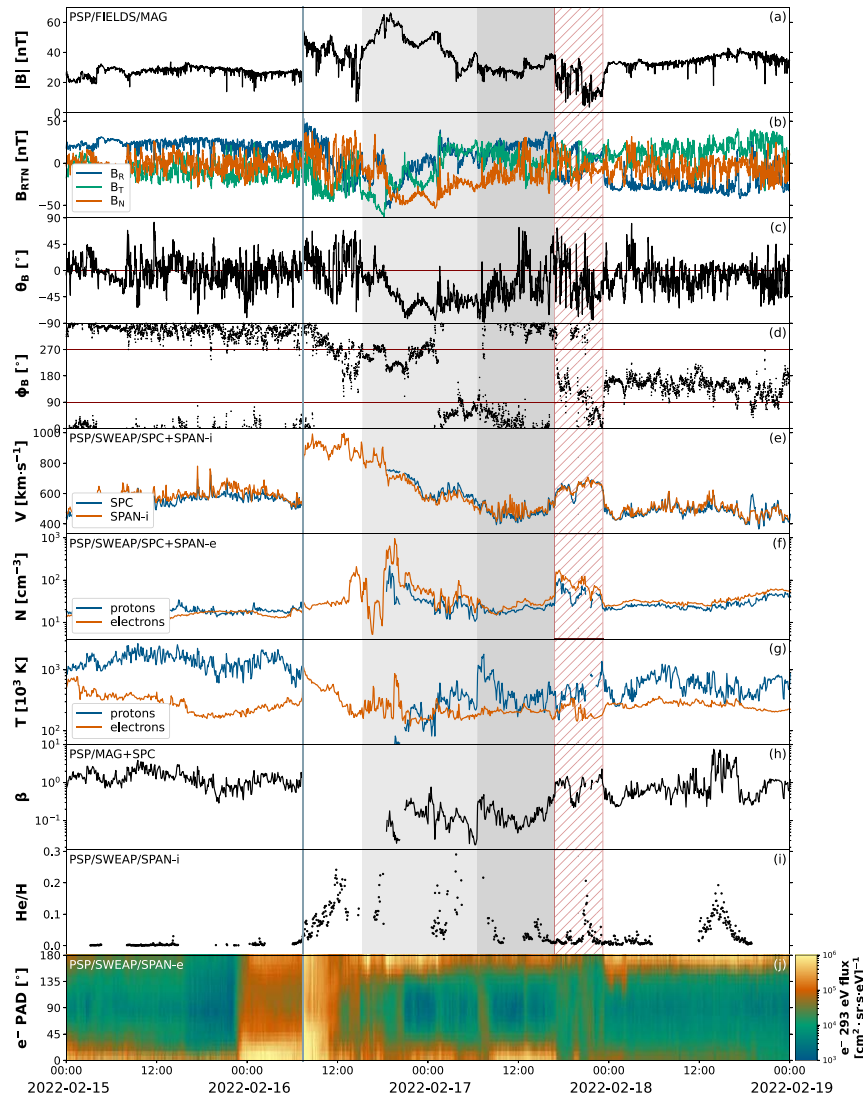
Figure 5. Overview of in situ data at Parker for the period 2022 February 15–18. The plot shows, from top to bottom: (a) magnetic field magnitude, (b) magnetic field Cartesian components in RTN coordinates, (c) latitudinal and (d) longitudinal angles of the magnetic field, (e) solar wind bulk speed, proton (f) density and (g) temperature, (h) plasma beta, (i) helium-to-proton ratio, and (j) pitch angle spectrogram of suprathermal 293 eV electrons. The vertical gray line indicates the arrival of the CME-driven shock, while the gray shaded areas highlight the magnetic obstacle (light+dark gray) and the magnetic cloud (light gray) within it. The hatched area marks the HPS passage immediately following the CME.

prominence material had elemental abundances that were less enhanced in the low first-ionization-potential species than the surrounding flux rope structure, suggesting more solar-wind-like elemental properties (Rivera et al. 2023).

Finally, we note a structure immediately following the ejecta characterized by a low magnetic field magnitude as well as enhanced speed, density, and plasma beta (hatched area in Figure 5). Additionally, both the longitudinal component of the magnetic field and the suprathermal electron PAD display a ∼180° reversal after the passage of this feature, compared to the pre-CME ambient wind. The structure shows all the typical characteristics of a heliospheric plasma sheet (HPS) crossing (e.g., Crooker et al. 2004; Lavraud et al. 2020), i.e., the passage of a high-density and high-beta region that surrounds the heliospheric current sheet. We tentatively associate the HPS at Parker (starting at ∼17:00 UT on February 17) with a similar structure (featuring a low magnetic field magnitude as well as a reversal of the longitudinal component of the field) detected at Bepi approximately 1 day later (starting at ∼17:00 UT on

February 18; see Figure 4), i.e., well after the passage of the 2022 February 15 CME. Hence, the (spatial and temporal) proximity of the HPS to the CME at Parker—and the resulting interaction between the two—may explain the presence of more ambiguous magnetic cloud and magnetic obstacle boundaries at Parker, which are, on the other hand, not found at Bepi.

4. Analysis of the Mesoscale CME Structure

In this section, we analyze in detail the similarities and differences related to observations of the 2022 February 15 CME at Bepi and Parker. We focus our investigation on the three main regions and/or features of in situ CMEs, i.e., the interplanetary shock, the sheath region, and the magnetic ejecta.

4.1. Interplanetary Shock

As mentioned in Section 3.1, an interplanetary shock was detected on 2022 February 16 at 06:25 UT by Bepi and 07:25 UT by Parker. Although it is not possible to determine

the passage of a shock with certainty at Bepi due to the lack of corresponding plasma data, the prominent nature of the shock at Parker (see Section 3.2), together with the spatial proximity of the two probes, allows us to proceed with our analysis under the assumption that both spacecraft measured the same feature.

When investigating the properties of interplanetary shocks, the first step is to define the plasma states upstream and downstream of the shock. In this work, the criteria for determining the upstream and downstream conditions are adopted from those used in the Heliospheric Shock Database[21] (Kilpua et al. 2015) and consist of averaging the quantities under consideration over 8 minute intervals that end 1 minute before and start 2 minutes after the identified shock passage time, i.e.,

$$
\begin{cases}
t_u = [t_{\mathrm{shock}} - 9 \text{ minutes}, \ t_{\mathrm{shock}} - 1 \text{ minute}] \\
t_d = [t_{\mathrm{shock}} + 2 \text{ minutes}, \ t_{\mathrm{shock}} + 10 \text{ minutes}],
\end{cases} \quad (2)
$$

where the subscript u indicates the upstream state and the subscript d indicates the downstream state. These intervals ensure that the mean upstream and downstream values are estimated sufficiently far from the shock ramp (and the particularly turbulent region in the immediate shock downstream). We remark, nevertheless, that the choice of the upstream and downstream windows may significantly affect the resulting shock parameters (e.g., Balogh et al. 1995; Trotta et al. 2022). Here, small variations in the interval selections had minimal impact on our calculated normals, but we did not perform an exhaustive parameter-dependency analysis. The various shock properties calculated for both Bepi (where possible) and Parker are summarized in Table 2, and they are described in detail below.

The first two shock characteristics reported in Table 2 are compression ratios, defined as

$$
r_X = \frac{X_d}{X_u}, \quad (3)
$$

where X indicates a general physical quantity—usually the magnetic field magnitude, B; the proton density, n_p; and/or the proton temperature, T_p. In the case of the event studied here, we report the magnetic compression ratio, r_B, for both Bepi and Parker, while for the density compression ratio, r_n, we use electron measurements at Parker as a proxy—generally, a reasonable approximation under the assumption of quasi-neutrality of the plasma—due to the lack of downstream proton data (see Figure 5). We note that r_B features identical values of 2.04 at the two spacecraft, while r_n is found to equal 1.80 at Parker. These compression ratios are usually considered as proxies for the strength of a shock (e.g., Burton et al. 1996; Oh et al. 2007), and their expected values have been found to not vary significantly between 0.3 and 1 au (Volkmer & Neubauer 1985; Lai et al. 2012). We find our compression ratios to be very similar to the median values detected by the Helios mission between 0.3 and 0.8 au—i.e., 1.84 for r_B and 1.87 for r_n (Pérez-Alanis et al. 2023)—indicating that the 2022 February 15 CME drove a shock of average strength. Nevertheless, studies have found that interplanetary shocks tend to be stronger in the proximity of their nose than along their flanks (e.g., Cane 1988; Kallenrode et al. 1993), suggesting that had the CME been

---

Table 2
Shock Parameters Derived for both Bepi and Parker

Shock Parameter	Bepi	Parker
Jumps		
r_B	2.04	2.04
r_n	…	1.80
ΔV	…	282 km s^{-1}
MCT		
$\hat{\boldsymbol{n}}_{\mathrm{MCT}}$	[0.76, 0.63, 0.16]	[0.45, −0.82, −0.37]
Θ_{MCT}	7°.3	31°.8
Λ_{MCT}	40°.5	63°.3
Ξ_{MCT}	9°.0	−21°.4
MVA		
$\hat{\boldsymbol{n}}_{\mathrm{MVA}}$	[0.57, −0.25, −0.78]	[0.53, −0.42, −0.73]
Θ_{MVA}	80°.4	42°.6
Λ_{MVA}	55°.0	57°.8
Ξ_{MVA}	−51°.3	−47°.1
λ_2/λ_3	3.07	2.71
B_n/B	0.15	0.45
MD3		
$\hat{\boldsymbol{n}}_{\mathrm{MD3}}$	…	[0.49, −0.71, −0.51]
Θ_{MD3}	…	33°.3
Λ_{MD3}	…	60°.9
Ξ_{MD3}	…	−30°.6

Note. r_B = magnetic compression ratio. r_n = density compression ratio. ΔV = velocity jump. $\hat{\boldsymbol{n}}$ = shock normal. Θ = shock angle. Λ = location angle. Ξ = elevation angle. λ_2/λ_3 = intermediate-to-minimum eigenvalue ratio. B_n/B = minimum-variance-to-total magnetic field ratio.

encountered closer to its apex (see Section 2.2 for an estimate of its propagation direction well north of the ecliptic), Bepi and Parker may have measured higher values for the corresponding compression ratios.

The next parameter reported in Table 2 is the shock speed jump, defined as

$$
\Delta V = V_d - V_u. \quad (4)
$$

As in the case of r_n, ΔV can be calculated at Parker only, resulting in a jump of 282 km s^{-1}. Although shocks driven by fast CMEs tend to slow down as they propagate through the inner solar system (e.g., Woo et al. 1985; Neugebauer 2013), this value is slightly higher than average, since shock jumps measured inside 1 au are usually below 200 km s^{-1} (Luhmann 1995). The high speed of the shock driven by the 2022 February 15 CME and detected at ∼0.35 au may be due to its propagation through a rarefied (∼20 cm^{-3}) and fast (∼600 km s^{-1}) solar wind stream (see Figure 5), which in turn hindered its deceleration due to drag effects.

The following parameters reported in Table 2 all concern the shock normal, $\hat{\boldsymbol{n}}$, and its related angles. Given the large uncertainties that are known to be associated with shock normal determination methods (e.g., Russell et al. 1983; Schwartz 1998), we compare in this work results using three techniques: the magnetic coplanarity theorem (MCT; Colburn & Sonett 1966), minimum variance analysis (MVA; Sonnerup & Cahill 1967), and the mixed-mode method (MD3; Abraham-Shrauner & Yun 1976). We note that, while MCT and MVA are based uniquely on magnetic field data and can hence be
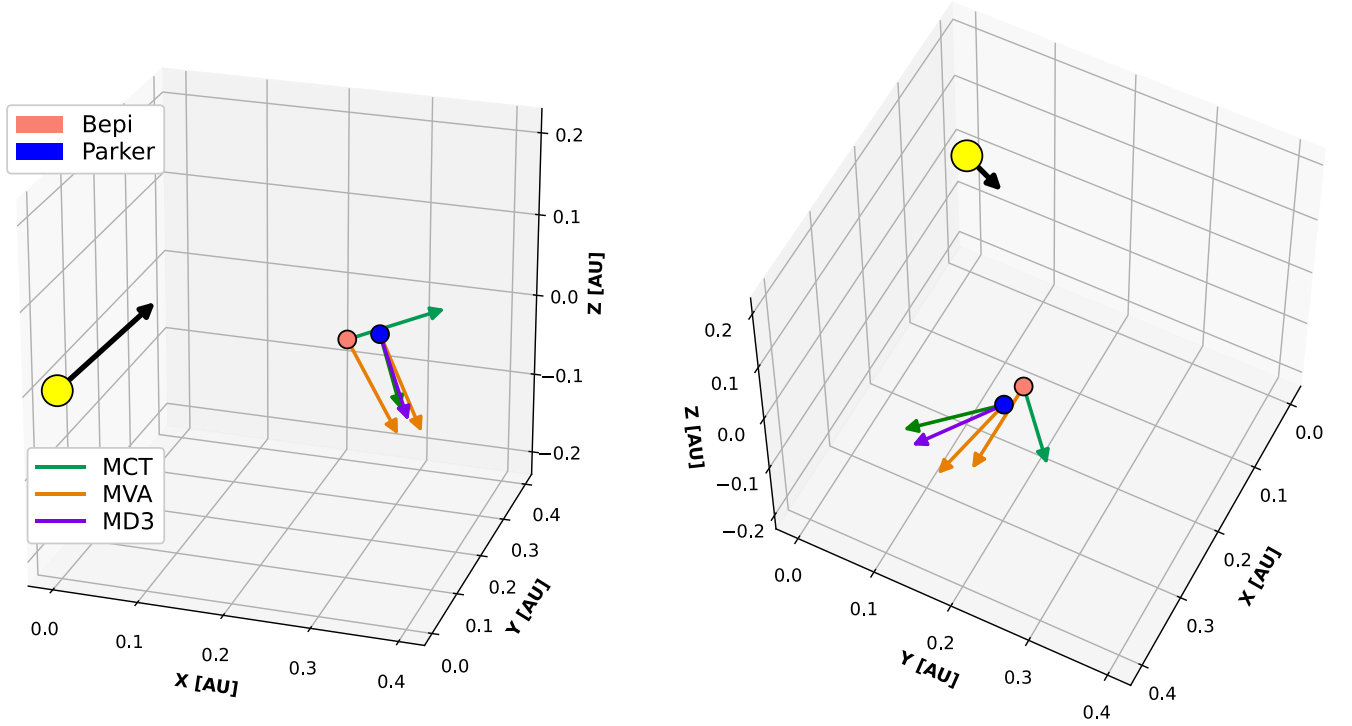
Figure 6. Overview of the shock normals calculated with different methods at both Bepi and Parker, shown from two different perspectives to provide a better insight into their orientations in 3D. Normals calculated with the MCP and MVA methods are displayed for both spacecraft, while the normal derived using the MD3 technique is presented for Parker only, since its derivation requires plasma data. The location of the Sun is represented with a yellow sphere, and the black arrow indicates the trajectory of the CME nose as derived from the GCS fitting shown in Figure 3.

applied to both probes, MD3 needs speed measurements and can thus be used at Parker only. The shock normals resulting from the different methods are visualized in 3D in Figure 6.

The MCT technique is based on the assumption that $\boldsymbol{B}_u$, $\boldsymbol{B}_d$, and $\hat{\boldsymbol{n}}$ lie in a single plane, and the shock normal is computed as

$$\hat{\boldsymbol{n}}_{\mathrm{MCT}} = \pm \frac{(\boldsymbol{B}_d - \boldsymbol{B}_u) \times (\boldsymbol{B}_d \times \boldsymbol{B}_u)}{|(\boldsymbol{B}_d - \boldsymbol{B}_u) \times (\boldsymbol{B}_d \times \boldsymbol{B}_u)|}. \quad (5)$$

The MVA technique assumes that, when a spacecraft crosses a "transition layer" (e.g., a shock front), the divergence-free nature of the magnetic field imposes the condition that the field component normal to such a layer is continuous. It solves the set of three equations for the eigenvectors and eigenvalues of the magnetic variance matrix

$$\sum_{\nu=1}^{3} M_{\mu\nu} n_\nu = \lambda n_\mu, \quad (6)$$

where $M_{\mu\nu} = \langle B_\mu B_\nu \rangle - \langle B_\mu \rangle \langle B_\nu \rangle$. The eigenvector associated with the smallest eigenvalue, λ_3, is the direction of minimum variance of the magnetic field and thus corresponds to the shock normal, $\hat{\boldsymbol{n}}_{\mathrm{MVA}}$. The reliability of the solution can be investigated via the intermediate-to-minimum eigenvalue ratio, λ_2/λ_3, and the minimum-variance-to-total magnetic field ratio across the discontinuity, B_n/B. Values of $\lambda_2/\lambda_3 \geqslant 2$ and $B_n/B \leqslant 0.3$ are usually considered to describe the shock normal as well defined (Lepping & Behannon 1980).

Finally, the MD3 technique expands upon the MCT one by incorporating velocity changes across the shock. This method is usually considered more robust than those that only use

magnetic field data, and the normal is calculated as

$$\hat{\boldsymbol{n}}_{\mathrm{MD3}} = \pm \frac{(\boldsymbol{B}_d - \boldsymbol{B}_u) \times ((\boldsymbol{B}_d - \boldsymbol{B}_u) \times (\boldsymbol{V}_d - \boldsymbol{V}_u))}{|(\boldsymbol{B}_d - \boldsymbol{B}_u) \times ((\boldsymbol{B}_d - \boldsymbol{B}_u) \times (\boldsymbol{V}_d - \boldsymbol{V}_u))|}. \quad (7)$$

Once the shock normals have been retrieved for each method and for each spacecraft, we calculate three angles related to them. The first is the shock angle, Θ, between the shock normal and the upstream magnetic field, defined as

$$\Theta = \arccos\left(\frac{|\boldsymbol{B}_u \cdot \hat{\boldsymbol{n}}|}{\|\boldsymbol{B}_u\|\|\hat{\boldsymbol{n}}\|}\right). \quad (8)$$

The second angle is the so-called location angle, Λ, between the shock normal and the radial direction (Janvier et al. 2014). It provides information as to the spacecraft crossing location with respect to the shock nose. Ideally, $\Lambda = 0°$ for a central encounter, and the larger the value (up to $|\Lambda| = 90°$), the farther the crossing location is from the apex. The angle can be computed as

$$\Lambda = \arctan\left(\frac{\sqrt{n_T^2 + n_N^2}}{n_R}\right). \quad (9)$$

The third and final angle is the elevation angle, Ξ, between the shock normal and the RT plane (in radial–tangential–normal, RTN, coordinates), defined as

$$\Xi = \arctan\left(\frac{n_N}{\sqrt{n_R^2 + n_T^2}}\right) = \arcsin\left(\frac{n_N}{\|\hat{\boldsymbol{n}}\|}\right). \quad (10)$$

According to the shock normal results shown in Table 2 and Figure 6, all the calculated normals point in a southeasterly way

($n_y < 0$ and $n_z < 0$) apart from the MCT case for Bepi, which points toward the northwest ($n_y > 0$ and $n_z > 0$). The shock is moderately quasi-parallel at Parker ($31° < \Theta < 43°$), while for Bepi, the MCT method retrieves a strongly quasi-parallel shock ($\Theta = 7°.3$), and the MVA technique produces a strongly quasi-perpendicular shock ($\Theta = 80°.4$). We note that quasi-parallel shocks are expected to occur more often closer to the Sun (<1 au), and quasi-perpendicular ones are more common at larger distances (~ 1 au) due to the configuration of the Parker spiral (e.g., Richter et al. 1985; Good et al. 2020). Regardless of the normal direction and nature of the shock, all the obtained location angles suggest spacecraft crossings considerably far from the shock nose ($40° < \Lambda < 65°$), as expected from our remote-sensing analysis of the 2022 February 15 CME (see Section 2).

While the normals retrieved at Parker are all in general agreement, we consider the ones retrieved with the MCT and MD3 methods to be more reliable, given the large value of the B_n/B ratio obtained with the MVA technique. At Bepi, on the other hand, both MVA ratios suggest a robust solution, which is in turn profoundly different from the one retrieved with the MCT method. Given the idealized (semispherical) shock geometry expected from the CME propagating to the northwest of the two probes (see Figure 6), it follows that the normal should indeed point approximately toward the southeast at the location of the spacecraft; thus, one may intuitively favor the MVA results. Additionally, the uncertainties associated with the MCT method are known to become larger the closer a shock is to being fully parallel or fully perpendicular (Viñas & Scudder 1986). However, given the prominent discrepancy between the two methods, we conclude that it is not possible to estimate a shock normal at Bepi in a reliable way. Nevertheless, it is clear that, despite the spatial proximity of Bepi and Parker, the two sets of measurements of the shock passage are dissimilar enough to produce fundamentally different results, possibly due to the shock being crossed significantly far from its nose and/or an irregular shock front (e.g., Koval & Szabo 2010; Kajdič et al. 2019) as well as the preexisting local conditions of the turbulent solar wind (e.g., Guo et al. 2021; Lavraud et al. 2021).

4.2. Sheath Region

The interplanetary shock detection was followed by a turbulent sheath region at both probes (see Figure 4). We identify the sheath passage on 2022 February 16 during 06:25–15:41 UT at Bepi and 07:25–15:18 UT at Parker, resulting in a duration of 9.3 hr at the former and 7.9 hr at the latter. We note that both these values are significantly larger than what is expected at Mercury's orbit, where sheath passages have been found to last on average 2.4 hr by Janvier et al. (2019) or 1.7 hr (2.2 hr) for fast (slow) CME drivers by Salman et al. (2020). A possible explanation for the observed long duration is that the CME was encountered by both probes close to its flank (as also confirmed by the interplanetary shock analysis in Section 4.1), since the thickness of a sheath is supposed to increase from the nose of the driving ejecta toward its sides (e.g., Gopalswamy et al. 2009; Kilpua et al. 2017). In such a case, Bepi would have encountered the CME farther from its nose than Parker. The mean (maximum) magnetic field magnitude measured in the sheath is 43.7 nT (69.8 nT) at Bepi and 38.8 nT (54.4 nT) at Parker, with values at both spacecraft being noticeably lower than the 57.8 nT (84.6 nT) determined

by Winslow et al. (2015) via a statistical analysis of 61 CMEs detected at Mercury's orbit. Again, a possible reason for the lower-than-average field strength is the probes' trajectory through the CME away from its nose.

As mentioned in Section 3.1, the sheath region is the part displaying overall the highest magnetic field fluctuations in the time series shown in Figure 4 for either probe. In contrast to superposed epoch analyses performed on sheaths detected at 1 au, which display a clear (absolute) maximum at the shock passage and a local maximum at the ejecta leading edge time (e.g., Masías-Meza et al. 2016; Kilpua et al. 2019a; Salman et al. 2021), the fluctuations observed at Bepi and Parker appear overall more uniformly distributed throughout the region. This may be due to the tendency for sheaths encountered closer to the Sun to generally display sharper field discontinuities and rotations (see, e.g., Good et al. 2020, who investigated the radial evolution of magnetic field fluctuation in sheath regions) or a result of passing through the flank of the CME. We remark, however, that statistical studies at 1 au often calculate B_{rms} over 1 minute time scales, while here we considered 15 minute intervals due to the available resolution of Bepi data for the period under analysis (see also Appendix B). We find the average B_{rms} over the whole sheath region to amount to 5.3 nT at Bepi and 4.5 nT at Parker. While this suggests a more turbulent sheath encountered at Bepi, it is important to bear in mind that this probe was closer to the Sun by ~ 0.03 au in radial distance. If we consider, instead, the normalized B_{rms}—obtained by dividing Equation (1) by the time-dependent magnetic field magnitude (B)—the average sheath fluctuations become ~ 0.13 at either spacecraft, indicating similar conditions in both sets of measurements.

To further analyze the fine structure of the sheath regions observed at the two spacecraft, we investigate the presence (or lack thereof) of planar magnetic structures (PMSs) using the algorithm of Palmerio et al. (2016). PMSs are structures in the solar wind characterized by abruptly changing magnetic field vectors that remain nearly parallel to a single plane (e.g., Nakagawa et al. 1989; Neugebauer et al. 1993) and are frequently found in CME-driven sheath regions (e.g., Palmerio et al. 2016; Ruan et al. 2023). In brief, the PMS search algorithm of Palmerio et al. (2016) first applies the MVA technique to the full sheath, verifying whether the PMS conditions of $\lambda_2/\lambda_3 \geqslant 5$ (e.g., Savani et al. 2011) and $B_n/B \leqslant 0.2$ (e.g., Jones & Balogh 2000) are fulfilled, in which case the entire region is considered planar. If one or both criteria are not matched, then the algorithm scans through the sheath region using a "sliding windows" procedure. At every iteration, the sheath duration is reduced by 5 minutes from its end part, and the shortened window is shifted back toward the ejecta leading edge with 5 minute increments, searching for the largest nonoverlapping intervals for which the PMS criteria hold (note that a single sheath may contain more than one PMS). In the work of Palmerio et al. (2016), which analyzed 95 sheaths observed near Earth, the minimum possible PMS duration was set to 1 hr. Here, to account for the fact that the structures under investigation were encountered at ~ 0.35 au, where sheaths are, on average, more modest in size, we allow for a minimum PMS duration of 30 minutes.

The results of the PMS analysis are shown in Figure 7 and Table 3. The PMS search algorithm finds one planar structure lasting approximately 1 hr at the center of each sheath. Despite
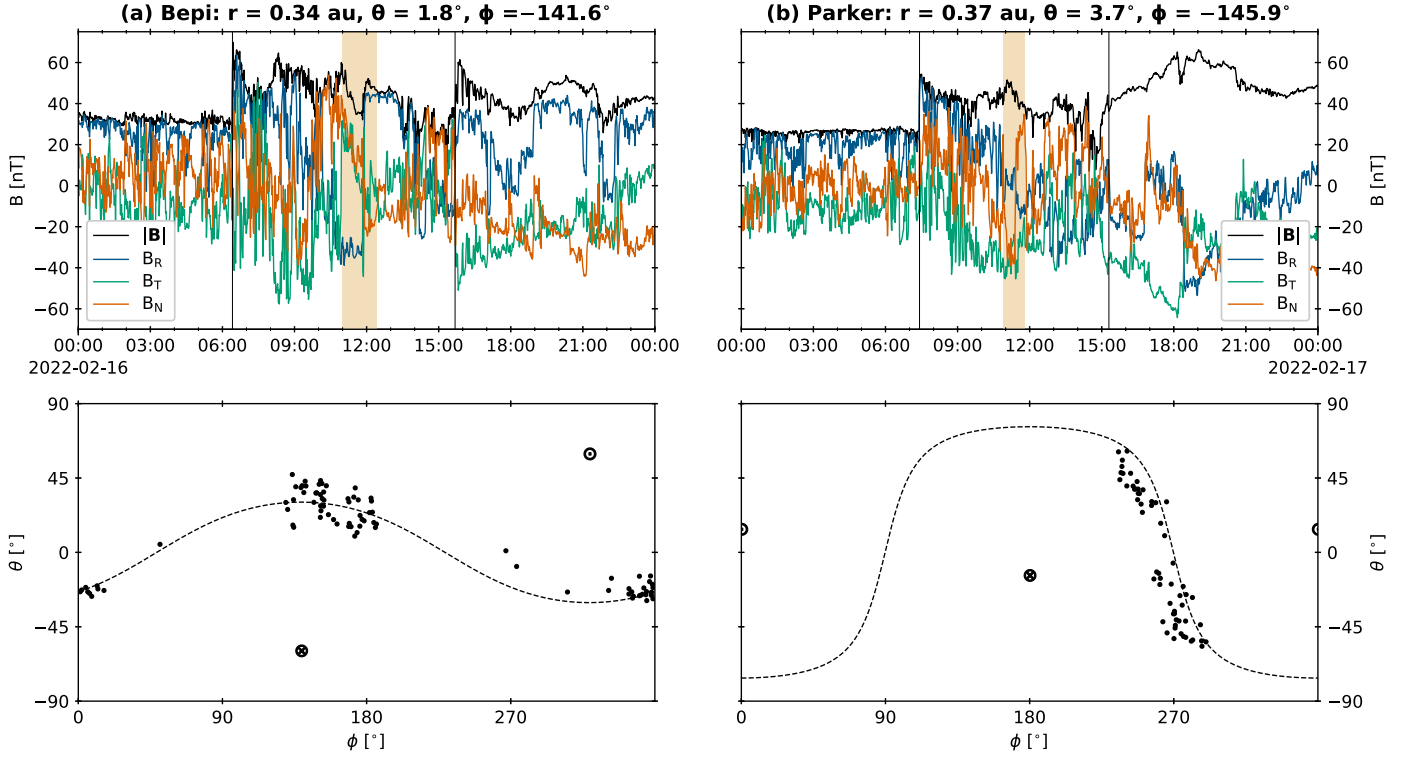
Figure 7. The PMSs identified in the sheath regions at (a) Bepi and (b) Parker. The top panels show magnetic field measurements around the time of the sheath region passage (marked by the two vertical lines), with the PMS interval highlighted in ocher. The bottom panels show the corresponding magnetic field vectors (within the PMS interval) on the θ–ϕ surface, with the dashed curve representing the PMS plane and the $\odot$ ($\otimes$) symbol indicating the normal direction out of (into) it.

Table 3
Results of the PMS Analysis at Bepi and Parker

PMS Property	Bepi	Parker
D [hr]	1.4	1.0
λ_2/λ_3	5.0	5.1
B_n/B	0.10	0.12
$O_{\rm PMS}$	(60°, 319°)	(14°, 360°)
$\hat{n}_{\rm PMS}$	[0.38, −0.33, 0.86]	[0.97, −0.00, 0.24]

Note. D = PMS duration. λ_2/λ_3 = eigenvalue ratio. B_n/B = magnetic field ratio. $O_{\rm PMS}$ = orientation of the PMS plane in (θ, ϕ) format. $\hat{n}_{\rm PMS}$ = normal vector to the PMS plane.

their similar duration and location within their respective sheath regions, the two PMSs display different plane orientations, with the one found at Bepi oriented toward the northeast and the one found at Parker nearly aligned with the Sun–spacecraft line. Additionally, we note that the presence of a PMS in the central region of a sheath is a rather uncommon occurrence (e.g., Palmerio et al. 2016), since planar structures are believed to form due to compression and alignment of discontinuities downstream of a shock (e.g., Jones et al. 2002) and/or due to magnetic field draping ahead of an ejecta (e.g., Kataoka et al. 2005). Nevertheless, the excellent agreement between their respective positions within the sheath as well as their temporal duration, suggests that the structures found at Bepi and Parker were the result of the same formation mechanism. Given the turbulent nature of the solar wind, especially in the downstream region of a shock, it is possible that the retrieved PMS orientations are deeply reflective of the local sheath conditions

and hence can vary more or less dramatically over relatively small spatial scales.

Indeed, this last point connects to the next step in our analysis, which is aimed at investigating the level of coherence of the sheath magnetic fields measured at the two spacecraft. To do so, we employ an approach similar to that used by Ala-Lahti et al. (2020), who analyzed the longitudinal spatial coherence of CME-driven sheath regions observed at 1 au by spacecraft characterized by nonradial separations between 0.001 and 0.012 au (0°06–0°69). Specifically, they computed the Pearson correlation coefficients (r) between each pair of magnetic field components as well as the field magnitude. In the case explored here, the spacecraft nonradial separation is ∼0.03 au, which corresponds to ∼5° at ∼0.35 au. We note that, while this relative distance is larger than the range explored by Ala-Lahti et al. (2020), it is well within the estimated scale lengths of typical magnetic field coherence in sheath regions resulting from their study (see also the discussion in the Introduction).

The results of the sheath magnetic coherence analysis are shown in Figure 8. To directly compare the two sheath regions, we have stretched (or, actually, "shrunk") the Bepi measurements onto the Parker ones by aligning both the shock and the ejecta leading edge passage times. This approach is slightly different from the one employed by Ala-Lahti et al. (2020), who examined the two magnetic field data sets using two methods. The first consists of maximizing the cross-correlation of a combined Pearson coefficient that takes into account the magnetic field magnitude as well as its components, and the second consists of simply aligning the two shock arrival times (without stretching one time series onto the other). We have computed our correlations using the shock-aligning approach
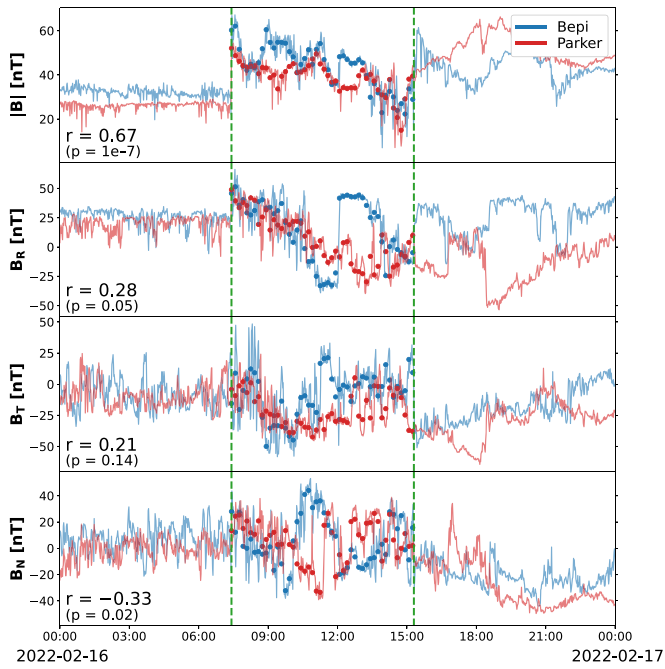
Figure 8. Magnetic field observations of the sheath region driven by the 2022 February 15 CME at Bepi and Parker. The Bepi measurements have been stretched to match the sheath duration at Parker and time-shifted to align the two shock arrival times. The dashed vertical green lines mark the beginning and end of the sheath region within which the magnetic field correlations are computed. The solid profiles show 1 minute measurements, while the scatter points indicate the 10 minute averaged data used to calculate the corresponding Pearson correlation coefficients (reported on the bottom left of each panel together with their *p*-values).

as well, and the results are qualitatively comparable to the ones displayed in Figure 8. The Pearson correlation coefficients emerging from our analysis are $[B, B_R, B_T, B_N] = [0.67, 0.28, 0.21, -0.33]$; hence, there is a good correlation in the magnetic field magnitude but weak-to-no correlation in the field components. These results are in contrast to the ones from Ala-Lahti et al. (2020), who reported the best correlation in the east–west component of the magnetic field (B_T) for sheath regions, with some degree of coherence maintained until ~ 0.15 au (or $\sim 9°$) at 1 au. In fact, they suggested that correlations in the total magnetic field (B), as well as its radial (B_R) and north–south (B_N) components, are expected to cease for separations larger than 0.04 au (or $\sim 2°$) at 1 au. The higher-than-expected degree of coherence that we found in B and B_R for a $\sim 5°$ separation at ~ 0.35 au might be related to the fact that changes in the sheath properties are known to increase with heliocentric distance as a CME propagates in interplanetary space (e.g., Salman et al. 2020; Winslow et al. 2021). On the other hand, the lower-than-expected degree of coherence that we found in B_T may be due to the different Parker spiral orientation at ~ 0.35 au when compared to 1 au—i.e., characterized by a significantly smaller component in the east–west direction.

Finally, we inspect the available plasma data from Parker (see Figure 5) to obtain a deeper insight into the sheath's structure and evolution, including the relationship with its driver. First of all, we focus on the speed profile measured within the sheath region and apply a linear regression to it, finding an overall decrease of $\sim 3\%$ from the interplanetary shock to the ejecta leading edge (speed decline by 26 km s^{-1} and average speed of 901 km s^{-1}), with a slope relative to the

average sheath speed of 0.37% hr^{-1}. The mean error associated with the regression, however, is 4.8% with respect to the average sheath speed, making the structure encountered at Parker akin to the "Category-D" sheaths of Salman et al. (2021), i.e., those characterized by a complex (nonlinear) speed profile. The statistical analysis of Salman et al. (2021) was centered on sheaths preceded by shocks encountered at 1 au, and, among their findings, the authors reported that Category-D sheaths tend to be driven by CMEs that are detected in situ far from their apex, as is indeed the case for the 2022 February 15 event.

Another interesting aspect to investigate is the contribution of CME propagation and expansion to the sheath formation— CME-driven sheaths, in fact, are considered "hybrid" structures that feature aspects of propagation sheaths, in which the solar wind flows around a propagating object, and expansion sheaths, in which the solar wind piles up ahead of an expanding object (e.g., Siscoe & Odstrcil 2008). To do so, we calculate two Mach numbers: M_{prop}, based on the ejecta propagation speed, and M_{exp}, based on the ejecta expansion speed (see Equations (1) and (2) in Salman et al. 2021 for a definition of the two parameters). The propagation speed is simply the ejecta average speed, $V_{prop} = 589$ km s^{-1}, while the expansion speed is defined as the half-difference between the speeds of the leading and trailing edges (Owens et al. 2005), $V_{exp} = 142$ km s^{-1}. We obtain $M_{prop} = 0.27$ and $M_{exp} = 0.82$, indicating that the sheath driven by the 2022 February 15 CME was mainly an expansion one. This is consistent with the presence of a PUC region immediately ahead of the ejecta leading edge (see the prominent density enhancement in the trailing portion of the sheath in Figure 5), usually attributed to strong CME overexpansion. In fact, the CME analyzed in this work might still have been experiencing significant expansion by the time it was detected at Parker, since the sheath appears overall less dense than the following ejecta, in agreement with Salman et al. (2021), who found that expansion sheaths tend to display lower densities, on average. Furthermore, Temmer & Bothmer (2022) estimated that the sheath density tends to overcome the ejecta density in the heliocentric distance range of 0.09–0.28 au, after which expansion of the driver generally weakens. We also note that Giacalone et al. (2023) came to the same conclusion (i.e., that the 2022 February 15 CME was overexpanding by the time it impacted Parker) by observing the intensity of energetic particle increase behind the shock, possibly resulting from ions filling an expanding volume associated with the propagation of a blast wave.

4.3. Magnetic Ejecta

The passage of the sheath region was followed by the arrival of the magnetic ejecta at both probes (see Figure 4). We determine the ejecta boundaries on 2022 February 16–17 during 15:41–07:51 UT at Bepi and 15:18–16:48 UT at Parker, noting that flux rope signatures at the latter spacecraft were identified until 06:32 UT on February 17 (see Section 3). These intervals result in ejecta durations of 16.2 hr at Bepi and 25.5 hr at Parker, i.e., significantly larger than the average of 7.2 hr reported by Janvier et al. (2019) for CMEs encountered at $\sim$ 0.4 au. The mean (maximum) magnetic field magnitude measured in the ejecta is 41.3 nT (61.4 nT) at Bepi and 45.9 nT (66.3 nT) at Parker, noting that values at both spacecraft are lower than the average values at Mercury's orbit of 55.3 nT (86.2 nT) as reported by Winslow et al. (2015).

Additionally, we note that both the mean and maximum field values at Parker are higher than at Bepi, despite the former being slightly farther from the Sun than the latter. This may be due to the longitudinal and latitudinal separation between the two probes (i.e., intrinsic differences in the CME structure over relatively short spatial scales) and/or the higher-speed wind following the ejecta at Parker, resulting in compression of the field. Overall, possible reasons for the longer durations and lower field magnitudes measured in the two ejecta investigated here in comparison to average values at Mercury are the fact that the event was encountered in situ only through its southern flank (see Section 2) as well as the strong expansion experienced by the CME—as mentioned in Section 4.2, we find an expansion speed (based on Parker measurements), $V_{\exp}$, of ~ 142 km s^{-1}. When considering the magnetic cloud interval only, the expansion speed is basically unchanged (~ 144 km s^{-1}), since the trailing portion of the ejecta features a plateau in the bulk velocity. These values are significantly higher than the average CME expansion speeds of ~ 30 km s^{-1} found at 1 au (e.g., Nieves-Chinchilla et al. 2018b; Lugaz et al. 2020), but it remains unclear what the corresponding "typical" expansion speeds at ~ 0.35 au may be due to the lack of systematic in situ plasma measurements, although it is generally assumed that CME expansion should somewhat decrease between the Sun and Earth's orbit (e.g., Wang et al. 2005; Zhuang et al. 2023).

To obtain an indication of the overall cross-sectional ejecta structure encountered by either probe, we evaluate the distortion parameter (DiP) introduced by Nieves-Chinchilla et al. (2018b). In brief, the DiP quantifies the level of distortion in a CME due to, e.g., interactions with the background solar wind by examining the measured profile of the magnetic field magnitude and is defined as the fraction of the full ejecta interval where 50% of the total B is accumulated. We find a DiP at Bepi of 0.48, while at Parker, we obtain DiP = 0.39 for the magnetic obstacle and DiP = 0.43 for the magnetic cloud interval. According to Nieves-Chinchilla et al. (2018b), events with DiP = 0.50 ± 0.07 can be considered symmetric in their magnetic field profile, which is the case for Bepi according to our results. For Parker, the magnetic obstacle interval features a DiP that is consistent with compression at the front and that, together with the high $V_{\exp}$ mentioned above, indicates that the asymmetric nature of the B profile is due to expansion of the structure as it crosses the spacecraft—also known as the "aging effect" (e.g., Démoulin et al. 2008). However, if we consider only the magnetic cloud portion of the ejecta at Parker, we find a DiP value that suggest an approximately symmetric profile alongside a high $V_{\exp}$. At the same time, it is unlikely that the large speed gradient (between the ejecta leading and trailing edges) found at Parker corresponds to a flat speed profile at Bepi. Nieves-Chinchilla et al. (2018b), in their study of 337 CMEs detected at 1 au, found only a few events characterized by $0.43 \leqslant \mathrm{DiP} \leqslant 0.57$ and $V_{\exp} \geqslant 100$ km s^{-1}, contradicting the expected effect of CME expansion on the magnetic field strength. It is unclear why this is the case here, but one possibility may be local distortions in the structure—see, e.g., how both sets of measurements in Figure 4 feature irregular profiles of the magnetic field magnitude, with several "bumps" across the ejecta passage, and how the plasma data at Parker in Figure 5 display complex trends in the density and temperature.

To evaluate the large-scale internal magnetic structure of the ejecta encountered at Bepi and Parker, we apply three different flux rope fitting models to the in situ magnetic field measurements. Specifically, we employ the force-free constant-α (FF; Lepping et al. 1990), the circular-cylindrical (CC; Nieves-Chinchilla et al. 2016), and the elliptic-cylindrical (EC; Nieves-Chinchilla et al. 2018a) analytical descriptions of flux ropes to recover geometric and magnetic parameters that allow us to estimate orientation, size, and flux content. All these methods require an average CME ejecta speed, for which we employ a value of 654 km s^{-1} based on the speed profile of the magnetic cloud portion at Parker (under the assumption that Bepi encountered similar velocities). Additionally, we employ the linear force-free self-similarly expanding (FE; Marubashi & Lepping 2007) cylindrical flux rope model, which is, in other words, an FF model that includes expansion. The FE technique requires fitting a full speed profile alongside the magnetic field components and thus is applicable in this case only to Parker data—here, we obtain our speed profile via a second-order polynomial fit to the in situ measurements. Results applied to the (full) ejecta at Bepi and the magnetic cloud portion of the ejecta at Parker are shown and summarized in Figure 9 and Table 4. The corresponding fits for the magnetic obstacle interval at Parker are reported and discussed in Appendix C.

We note that, despite the different fits appearing consistent overall at either spacecraft from visual inspection of Figure 9, the results reported in Table 4 display some stark differences in terms of both geometric and magnetic parameters. Nevertheless, we can extrapolate some common trends. For example, all techniques recover a right-handed flux rope at both probes (as expressed by the positive helicity sign, H), determine a higher axis inclination at Bepi when compared to Parker (as expressed by the latitude angle, ϑ_0), and estimate a more central encounter at Parker as opposed to Bepi (as expressed by the impact parameter, p_0). It has been shown that flux rope fitting results using different techniques can feature some disagreement even in "simple" cases characterized by negligible expansion speeds and symmetric magnetic field strength profiles (e.g., Al-Haddad et al. 2018); hence, it is not surprising to find discrepancies in this complex flank encounter event. One example can be seen in the B_R profiles shown in Figure 9, which display, on average, opposite polarities at the two spacecraft. If a different flux rope model were used that fit the B_R component with a more linear profile (such as the uniform-twist geometry; e.g., Farrugia et al. 1999), there could perhaps be less disagreement between the orientations obtained for each spacecraft. Nevertheless, flank encounter trajectories tend to be especially challenging for all in situ flux rope models (see the "problematic cases" discussed by Lynch et al. 2022). Overall, the most important conclusion to draw is that each of the flux rope models, when considered individually, returns very different "best-fit" parameter sets for the large-scale structure observed at Bepi and Parker, reflecting the significant differences in the (local) magnetic field time series measured within the ejecta by each spacecraft. We remark that the same holds true when considering the magnetic obstacle interval at Parker, as seen in the results presented in Appendix C.

To further investigate the coherence of the magnetic fields measured by the two probes, we analyze the corresponding correlations in the observed time series by adopting a similar approach to Lugaz et al. (2018), who compared the ejecta of CMEs measured near 1 au over nonradial separations of 0.005–0.012 au ($0°.29$–$0°.69$). As was the case for the coherence analysis in the sheath, the nonradial separation
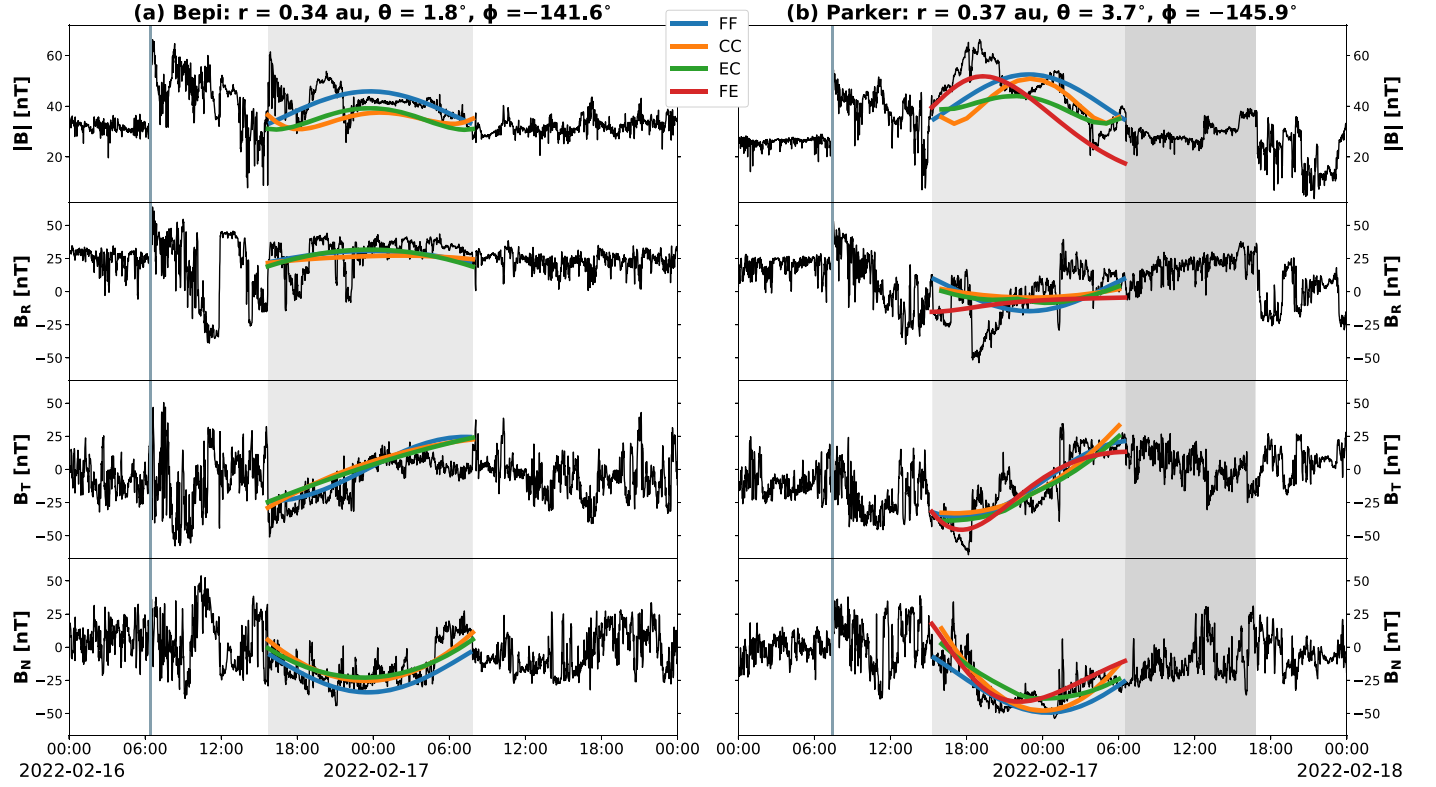
Figure 9. Flux rope fitting results at (a) Bepi and (b) Parker, showing magnetic field data at each spacecraft and the corresponding quantities resulting from different flux rope models. Note that, at Parker, the fitting is applied to the magnetic cloud interval only (see Appendix C for the corresponding results when considering the full magnetic obstacle).

between Bepi and Parker of ∼0.03 au (∼5°) during 2022 February 16–17 is larger than the range explored by Lugaz et al. (2018) but falls well within the typical scales of magnetic field coherence emerging from their study (see also the discussion in the Introduction). The results of our analysis are shown in Figure 10. In their study, Lugaz et al. (2018) aligned the magnetic field profiles by calculating the lag between the pairs of data that maximized the Pearson correlations, with the lags being computed separately for the field magnitude and each of the three components. Here, on the other hand, we adopt the time series stretching approach that we employed for the sheath region in Section 4.2, allowing us to directly compare the magnetic fields measured at Bepi with those detected at Parker in the magnetic cloud (Figure 10(a)) as well as in the magnetic obstacle (Figure 10(b)) intervals. By doing so, we find an intriguing result. In fact, the Pearson correlation coefficients are $[B, B_R, B_T, B_N] = [0.48, -0.02, 0.68, 0.28]$ when considering the Parker magnetic cloud only but change dramatically into $[B, B_R, B_T, B_N] = [0.08, 0.40, 0.82, 0.60]$ when computed over the Parker magnetic obstacle interval. Hence, for the magnetic cloud, we find good correlation in B_T, moderate correlation in B, and weak-to-no correlation in B_R and B_N, while for the magnetic obstacle, we obtain moderate-to-strong correlation in all the components with no correlation in the magnitude.

These results are in contrast to the ones from Lugaz et al. (2018), who found the greatest correlations in the magnetic field strength (B) and estimated that some degree of coherence should be maintained up to separations of 0.25–0.35 au (15°– 21°) at 1 au; for the single components, typical coherence scales instead lie between 0.07 and 0.12 au (4°–7°). According

to our results, the highest degree of coherence is obtained in the east–west (B_T) component regardless of the interval considered at Parker, and in the case of the magnetic obstacle interval, it is possible to encounter no correlation in the field magnitude, while at the same time, the single components all display moderate-to-strong agreement. A reasonable explanation for the generally lower-than-expected degree of coherence found in the 2022 February 15 event is that the CME was encountered far from its nose and with a high impact parameter by both spacecraft and thus considerably away from the stronger, possibly more ordered inner layers of the embedded flux rope. Furthermore, we note that Lugaz et al. (2018) deemed the correlation coefficient for the radial component of the magnetic field (B_R) ill-defined due to the lack of variation that is often observed along the Sun–observer line in flux-rope-like magnetic obstacles. In the event studied here, B_R is comparable in intensity to the other components; hence, its lower correlation coefficient when compared to B_T and B_N (regardless of the interval under consideration at Parker) appears to be due to intrinsic differences between the two ejecta—at Bepi, B_R is predominantly positive, while the opposite holds true at Parker. Again, this may be due to the glancing nature of the spacecraft encounters under investigation.

The magnetic field correlation analysis reported above suggests that, indeed, the "longer" interval that we considered at Parker corresponds to the "original," full CME ejecta. Nevertheless, from all the instances in which these data are shown (Figures 4, 5, 9, and 10), it is clear that there is a transition between the two distinct magnetic field environments of what we have defined as the magnetic cloud and the trailing portion of the magnetic obstacle. In Section 3.2, we tentatively

Table 4
Flux Rope Fitting Results at Bepi and Parker

Flux Rope Parameter	FF		CC		EC		FE
	Bepi	**Parker**	**Bepi**	**Parker**	**Bepi**	**Parker**	**Parker**
H	+1	+1	+1	+1	+1	+1	+1
ϑ_0 [deg]	−78.8	−29.0	−72.5	−66.8	−63.4	−51.1	−53.2
φ_0 [deg]	167.5	190.8	64.0	251.7	15.0	233.1	290.7
B_0 [nT]	63.8	66.5	60.1	51.0	50.3	43.8	76.2
R_0 [au]	0.166	0.074	0.165	0.108	0.145	0.115	0.101
p_0 [R_0^{-1}]	0.681	0.573	0.715	0.052	0.588	0.178	0.396
τ [au^{-1}]	5.21	11.69	0.53	0.95	0.71	2.05	8.54
Φ_{ax} [10^{21} Mx]	5.35	1.10	6.31	2.31	3.91	1.21	2.39
Φ_{po} [10^{21} Mx au^{-1}]	9.89	4.57	5.94	3.97	4.87	3.76	7.20
C1	⋯	⋯	1.71	1.42	1.50	0.96	⋯
ψ [deg]	⋯	⋯	⋯	⋯	19.4	74.3	⋯
δ	⋯	⋯	⋯	⋯	0.96	0.54	⋯

Note. H: helicity sign (or chirality); ϑ_0: axis latitude; φ_0: axis longitude; B_0: axial magnetic field magnitude; R_0: flux rope radius; p_0: normalized impact parameter; τ: twist; Φ_{ax}: axial flux; Φ_{po}: poloidal flux; C1: ratio of the azimuthal-to-axial current at the flux rope outer boundary; ψ: propagation angle (i.e., rotation around the flux rope axis); δ: cross-sectional distortion (equals 1 for a circular cross section and 0 for maximum distortion). The assumed average speed for the CME ejecta in the FF, CC, and EC fits is 654 km s^{-1}, while the FE procedure uses a polynomial fit to the observed speed profile.

attributed these features to magnetic flux erosion, which is a consequence of CME reconnection with the surrounding solar wind. Here, we investigate whether this is indeed the case. Figure 11 provides an overview of the results emerging from our analysis aimed at quantifying the amount of poloidal flux eroded due to reconnection in the interplanetary medium (i.e., shortly before the CME was detected in situ). These results employ as input outputs from the EC model, which allows for elliptical, distorted cross sections and thus has more degrees of freedom than the remaining two techniques showcased in Figure 9; we remark that we have repeated the same analysis, instead using the FF model that includes self-similar expansion, i.e. the FE model, and the results are very well consistent with the EC ones. Once geometric parameters (from any fitting model) such as flux rope axis direction, radius, and impact parameter are provided, we calculate the inbound–outbound flux asymmetry using the "direct method" of Dasso et al. (2005) as described in Pal et al. (2022). We perform these computations for both the magnetic cloud (Figure 11(a)) and the full magnetic obstacle (Figure 11(b)) intervals. According to the results shown in Figure 11, flux asymmetry is found at the back of the ejecta in both cases, indicating reconnection and erosion at the front of the rope (see the scenario depicted in Figure 6 of Pal et al. 2022). The asymmetry starts on 2022 February 17 at 05:25 UT (08:35 UT), and the eroded poloidal flux is 1.4×10^{21} Mx au^{-1} (1.5×10^{21} Mx au^{-1}) for the shorter (longer) interval (noting, however, that the glancing nature of the encounter may introduce additional errors in the results; e.g., Ruffenach et al. 2015). Our "by-eye" estimate of such a boundary fell on February 17 at 06:32 UT, i.e., comfortably in between the two times obtained with the flux erosion computation method. Thus, what emerges from this investigation is that the ejecta encountered at Parker was eroded, which may explain (at least in part) some of the differences in the structures encountered at the two spacecraft.

5. Discussion

The analysis and results presented in Section 4 reveal a series of similarities but also differences in the local measurements of the 2022 February 15 CME from Bepi and Parker, despite their relative proximity ($\sim$0.03 au in radial distance and $\sim$5° in nonradial separation). The eruption responsible for the event observed in situ was an impressive filament eruption that resulted in a fast ($\sim$2200 km s^{-1}) CME (see Mierla et al. 2022), observed in remote-sensing imagery to propagate with a significant northward component and thus expected to impact any in situ, near-the-ecliptic location through its southern flank. Here, we shall summarize the main findings with respect to the main structures that have been investigated, namely, the interplanetary shock, the sheath region, and the magnetic ejecta.

Analysis of the CME-driven interplanetary shock (Section 4.1) revealed that the two data sets featured an equal magnetic compression ratio, but determination of the shock normal and related parameters was inconsistent between the two probes. While at Parker, the three employed methods (MCT, MVA, and MD3) were generally in agreement in determining a moderately quasi-parallel shock with its normal pointing approximately toward the southeast, at Bepi, the two adopted techniques (MCT and MVA, since the plasma data necessary for MD3 were not available) provided two extremely different results: one suggesting a strongly parallel shock and the other indicating a strongly perpendicular one, with contrasting normal directions. It is interesting to note that the MVA method at the two spacecraft provided shock normal directions that are almost identical but resulted in an intermediate shock at Parker and a perpendicular one at Bepi. Overall, we concluded that the shock properties at Parker were at least qualitatively well defined, while at Bepi, it was not possible to obtain reliable results. It is likely that availability of plasma data at Bepi would have aided in the solution of the encountered discrepancies; apart from allowing determination of other properties such as density compression ratio and velocity jump, including speed changes across the discontinuity in shock normal estimations is known to provide more robust results. The shock normal directions determined using all methods at Parker and MVA at Bepi—i.e., roughly southeasterly—were at least consistent with the idealized scenario of a bubble-like shock surface that propagated to the northwest of the in situ observers.

Analysis of the CME-driven sheath region (Section 4.2) showed that the two spacecraft detected a comparable amount of magnetic field fluctuation, on average, indicating similar conditions of the corresponding magnetic environment. Another
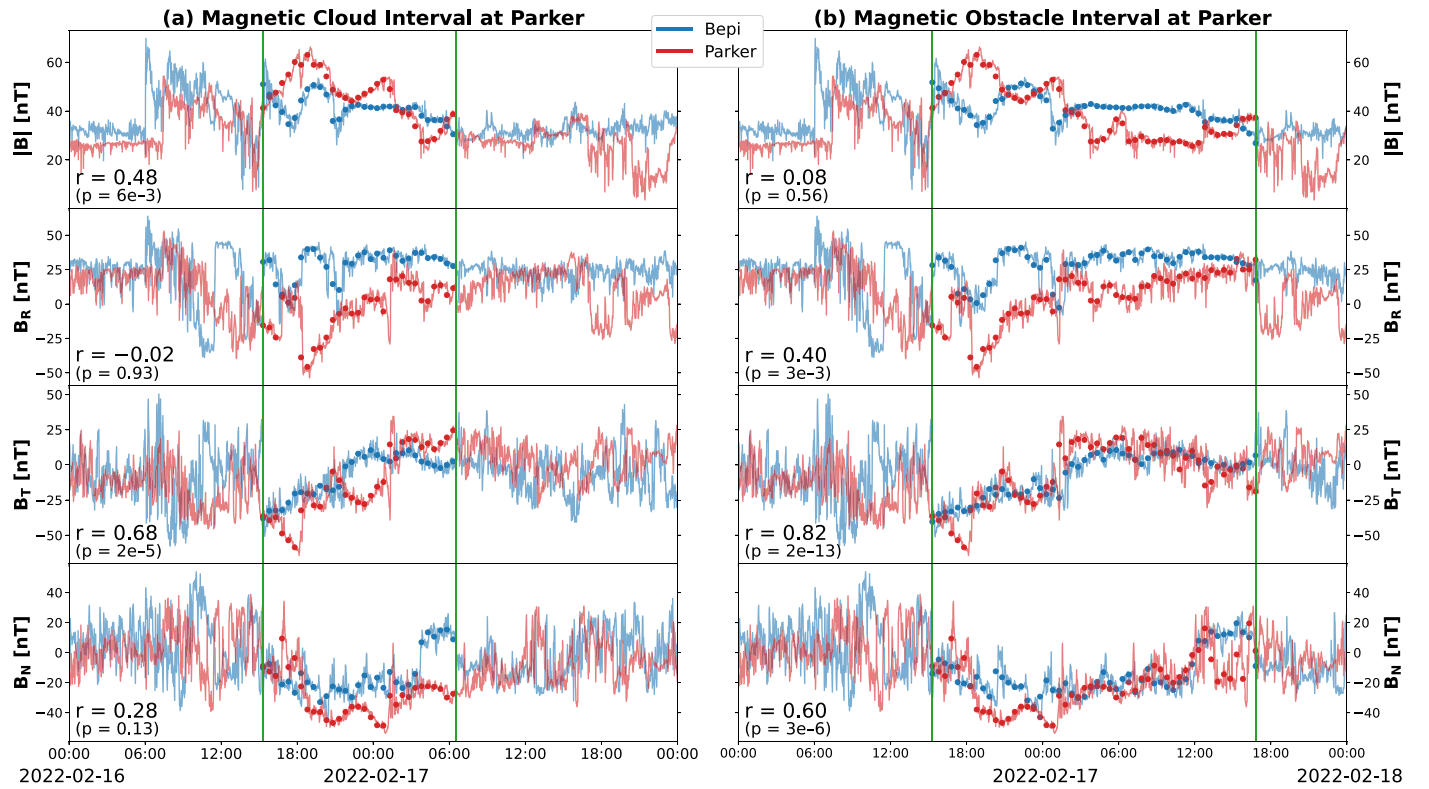
Figure 10. Magnetic field observations of the 2022 February 15 CME ejecta at Bepi and Parker. The Bepi measurements have been stretched to match the durations of (a) the magnetic cloud and (b) the magnetic obstacle at Parker and time-shifted to align the two ejecta leading edge times. The dashed vertical green lines mark the leading and trailing edges within which the magnetic field correlations are computed. The solid profiles show 1 minute measurements, while the scatter points indicate the 30 minute averaged data used to calculate the corresponding Pearson correlation coefficients (reported on the bottom left of each panel together with their p-values).

encountered similarity was that both sheaths had a PMS embedded in the middle, although the resulting PMS plane displayed different orientations. We speculated that the PMSs at the two probes formed via the same mechanism, and that the obtained orientations reflected the turbulent nature of the local (pre-shock-passage) solar wind. A direct comparison of the magnetic field measurements within the two sheath region data sets showed good correlation in the field magnitude but weak-to-no correlation in the field components. It is well known that CME-driven sheaths are highly fluctuating structures (e.g., Moissard et al. 2019; Kilpua et al. 2020); hence, variations over relatively close locations may be expected. For example, Kilpua et al. (2021) found, in a sheath measured at 1 au over distances of 0.01 au in the radial direction, 0°.5 in latitude and 1°.4 in longitude, different sheath durations, different numbers and positioning of magnetic field discontinuities within the sheath, and even different locations within the structure of an embedded small-scale flux rope. A more complete understanding of sheath region formation, evolution, and 3D variation will require multispacecraft in-depth analyses of CME-driven sheaths during periods featuring radially and/or longitudinally aligned probes (e.g., Good et al. 2020; Salman et al. 2020).

Analysis of the CME magnetic ejecta (Section 4.3) showed a single, relatively coherent structure at Bepi but a "two-part ejecta" at Parker; we identified the leading portion as the magnetic cloud (corresponding to the "core" flux rope) and the higher-fluctuating trailing part as a reconnected (open) field signature of erosion at the front of the ejecta. We employed different flux rope fitting techniques to recover geometric and magnetic properties of the ejecta measured at Bepi and Parker —considering both the magnetic cloud and the full magnetic obstacle intervals at the latter—and found more or less

dramatic differences not only between the different models but also between the two spacecraft within a single model. It is well known that different flux rope fitting models applied to the same data set may display significant discrepancies, especially in the case of flank encounters with high impact parameters (e.g., Riley et al. 2004; Al-Haddad et al. 2013). In the case investigated here, one may have expected better agreement due to the measurements being taken significantly closer to the Sun than 1 au, i.e., where less CME evolution has occurred. However, Lynch et al. (2022) showed that flux rope fitting models perform generally worse for flank encounters even as close as $10-30\,R_\odot$ using results from a magnetohydrodynamic model, which are characterized by smoother fields and do not fully reproduce the highly turbulent nature of the solar wind. Nevertheless, most fitting techniques (with the notable exception of the FF model at Parker) recovered a high-inclination flux rope, in agreement with GCS reconstruction results based on remote-sensing coronagraph observations (see Figure 3) and suggesting that the CME as a whole largely maintained its orientation as it traveled to ~0.35 au. The magnetic field correlation analysis between the two ejecta (comparing Bepi with both ejecta "options" at Parker) showed the highest agreement for the B_T component, while correlation in the field strength and the remaining two components varied depending on the ejecta interval under consideration at Parker. In particular, it was interesting to observe moderate-to-high correlation in all the components, but no correlation in the magnitude for the magnetic obstacle interval at Parker.

Overall, our investigation of the 2022 February 15 CME measured in situ at two relatively close spacecraft revealed some significant (local) variations of its large-scale structure. For example, the dramatically different duration of the ejecta interval
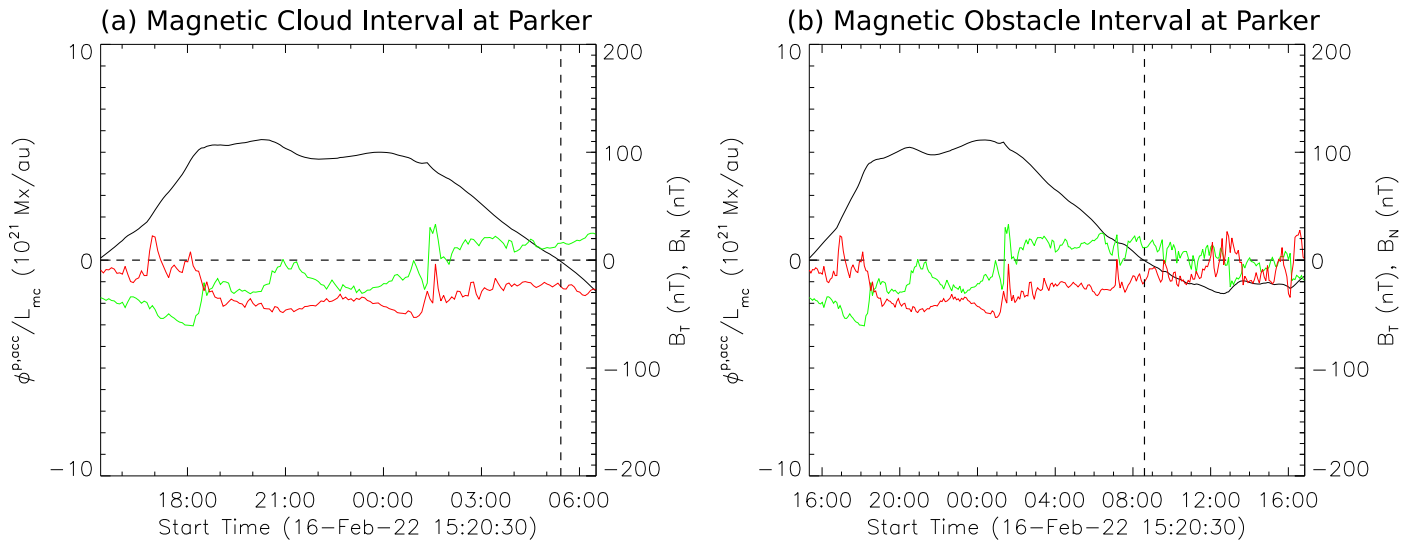
Figure 11. Overview of the flux erosion analysis for the 2022 February 15 CME ejecta at Parker, showing the time series of the accumulated poloidal flux (black) as well as the magnetic field components B_T (green) and B_N (red). The same analysis is performed for the (a) magnetic cloud and (b) magnetic obstacle intervals. The dashed vertical line marks the time at which flux asymmetry is estimated to begin.

—16.2 hr at Bepi and 25.5 hr at Parker, for a total difference of 9.3 hr—cannot be explained uniquely in light of CME expansion for a radial separation between the two probes of 0.03 au. We note that Regnault et al. (2024) reached the same conclusion for an event observed at SolO and Earth (separated at the time by 0.13 au in heliocentric distance and ∼2° in angular distance), highlighting how small spatial separations can have a prominent impact on the observed CME properties. Likewise, the different flux rope orientations recovered via fitting models (keeping in mind, however, the large uncertainties involved, especially at Bepi, due to the extra data processing described in Appendix B) suggest, in agreement with previous work (e.g., Farrugia et al. 2011; Möstl et al. 2012; Pal et al. 2023), that the axial field direction is more of a "local" quantity rather than part of a coherent, large-scale flux tube. In the case analyzed here, it is possible that interaction with a following HPS had some influence on the orientation of the ejecta at Parker as, e.g., the events investigated by Farrugia et al. (2011) and Pal et al. (2023) involved interactions with stream interaction regions or those studied by Möstl et al. (2012) involved CME–CME interactions. Finally, it is interesting to speculate on the uniqueness of the 2022 February 15 event that is the focus of this work. At both probes, we found average shock strengths, as well as longer durations and lower magnetic field magnitudes in both the sheath and ejecta when compared to typical values measured at Mercury's orbit. The strong expansion that we found based on Parker observations is in agreement with Scolini et al. (2021), who found that CMEs tend to expand rapidly until 0.4 au and shift to a more moderate growth rate at larger distances. Altogether, these features are consistent with those of a rather strong CME encountered toward its flank, where magnetic and kinematic properties are generally weaker. A follow-up investigation that could significantly complement the present work should compare these results with observations of a central, near-nose encounter under similar positioning conditions of the involved spacecraft. It is possible, in fact, that sampling two close-by trajectories closer to a flux rope central axis would result in much more consistent in situ data sets that would in turn inform us as to the expected coherence of CMEs across their full 3D structure. However, such a study would have to rely, as this one, on a fortuitous spacecraft conjunction together with a CME launched in a near-optimal direction, the likeliness of which can be estimated at the moment only in probabilistic terms.

6. Summary and Conclusions

In this work, we have analyzed in detail for the first time the mesoscale structure of a CME that was detected at Mercury's orbit by two different probes, i.e., Bepi and Parker, that were separated by ∼0.03 au in radial distance, ∼2° in latitude, and ∼4° in longitude (corresponding to a 3D separation of 0.0416 au or ∼8.95 $R_\odot$). We have focused on characterizing and comparing properties of the interplanetary shock, sheath region, and magnetic ejecta as measured by the two spacecraft. Overall, we have found some similarities but also some profound differences between the two sets of in situ data that, although resulting from flank encounters with the structure as a whole, are characterized by a relative nonradial angular separation (∼5°) that is smaller than the typical errors associated with 3D reconstructions of CMEs based on remote-sensing data—for example, Verbeke et al. (2023) found minimum uncertainties of 6° in latitude and 11° in longitude using the GCS model, and Kay & Palmerio (2024) estimated a typical difference of 4° in latitude and 8° in longitude between two independent reconstructions of the same event.

Ultimately, the findings of this work resonate with the conclusions and recommendations outlined by Lugaz et al. (2018), i.e., that the mesoscale range of the parameter space is still left largely unexplored in the context of CMEs, resulting in a knowledge gap over radial separations of 0.005–0.050 au and longitudinal separations of 1°–12° (i.e., the expected size of the cross section of a CME ejecta at 1 au). Even more so, the work reported here shows that the results of Lugaz et al. (2018) and Ala-Lahti et al. (2020) apply even at shorter heliocentric distances than 1 au, despite the generally smaller number of evolutionary processes such as interactions and deformations that are expected to have taken place. Fortunately, the importance of investigating mesoscales in the solar wind has been gaining more traction in recent years (e.g., Viall et al. 2021), and novel missions are being proposed to investigate variations and variability of solar transient events (e.g., Allen et al. 2022; Lugaz et al. 2023; Nykyri et al. 2023). The

potential benefits of a constellation of spacecraft designed to explore the mesoscale region would be invaluable for improving upon our knowledge not only of the fundamental physics of CMEs but also of other transient phenomena such as stream interaction regions and solar energetic particles.

The findings of this work also have implications in space weather research and operations. First of all, we remark on the importance of improving upon the available remote-sensing observations for trajectory and size determination of CMEs, since in situ measurements can show some prominent variability over short spatial scales. This could be achieved by increasing the number of operational telescopes in space and/or by observing the Sun and its environment from novel viewpoints, such as from outside the ecliptic plane (e.g., Gibson et al. 2018; Palmerio et al. 2023a; DeForest et al. 2023; Howard et al. 2023). From a modeling and forecasting perspective, we highlight the importance of considering "swarms" of virtual spacecraft (around Earth or the target body of interest) when generating predictions, with separations of the synthetic probes of even as little as $5°$ in nonradial distance to properly account for uncertainties in the physical processes that are being simulated as well as in the determination of CME input parameters from observations (e.g., Scolini et al. 2019; Asvestari et al. 2021; Palmerio et al. 2023b; Maharana et al. 2023). Additionally, this work showcased the need for reaching a better understanding and improving predictions of CME-driven sheath regions—an effort that was only in its infancy at the time of writing (e.g., Kay et al. 2020).

The relevance of this work to space weather research is not limited to improving predictions at Earth but also has applications for planetary science. The event studied here was encountered in situ by two spacecraft at Mercury's orbit, allowing us to analyze its characteristics at heliocentric distances that are significantly closer to the Sun than 1 au. Understanding the structure and evolution of CMEs within Mercury's orbit, in fact, is of high importance for the success of Bepi after its planned Mercury orbital insertion, as solar eruptive transients are the sources of many of the planetary dynamics on which the mission will focus (e.g., Milillo et al. 2020). Our knowledge of space weather at Mercury, including solar wind interaction with the Hermean magnetosphere, is at the moment rather limited, although some progress has been achieved via data collected during a few flybys (e.g., from Mariner 10) and orbital measurements from MESSENGER (e.g., Killen et al. 2004; Winslow et al. 2017). Future observations from Parker, SolO, and Bepi (cruise phase) of CMEs at Mercury's orbit in the solar wind, as well as from Bepi at Mercury after orbital insertion, will greatly enhance our understanding of space weather phenomena at the first planet from the Sun.

Finally, this analysis has been possible due to a fortuitous relative configuration of two probes, Bepi and Parker, at a time during which a remarkable CME was fortuitously launched in their direction. Even though such events are understandably rare, taking advantage of these "special kinds" of multispacecraft encounters, i.e., characterized by small radial *and* angular separations, is a concrete strategy that can be applied at present, at least while we wait for one or more dedicated missions to help characterize the solar wind and its transients over all the relevant spatial scales.

Appendix A
CME Observations by the WISPR Cameras On Board Parker

Observations of the 2022 February 15 CME captured by the WISPR Inner (field of view from $13°.5$ to $53°.0$) and Outer (field of view from $50°.0$ to $108°.0$) cameras on board Parker are part of the observing sequence scheduled for the spacecraft's Encounter 11 (E11) with the Sun, with perihelion on 2022 February 25 at 13.3 $R_\odot$. An overview of the Sun–WISPR observing geometry, available data, and science achievements during E11 has been provided by Liewer et al. (2023).
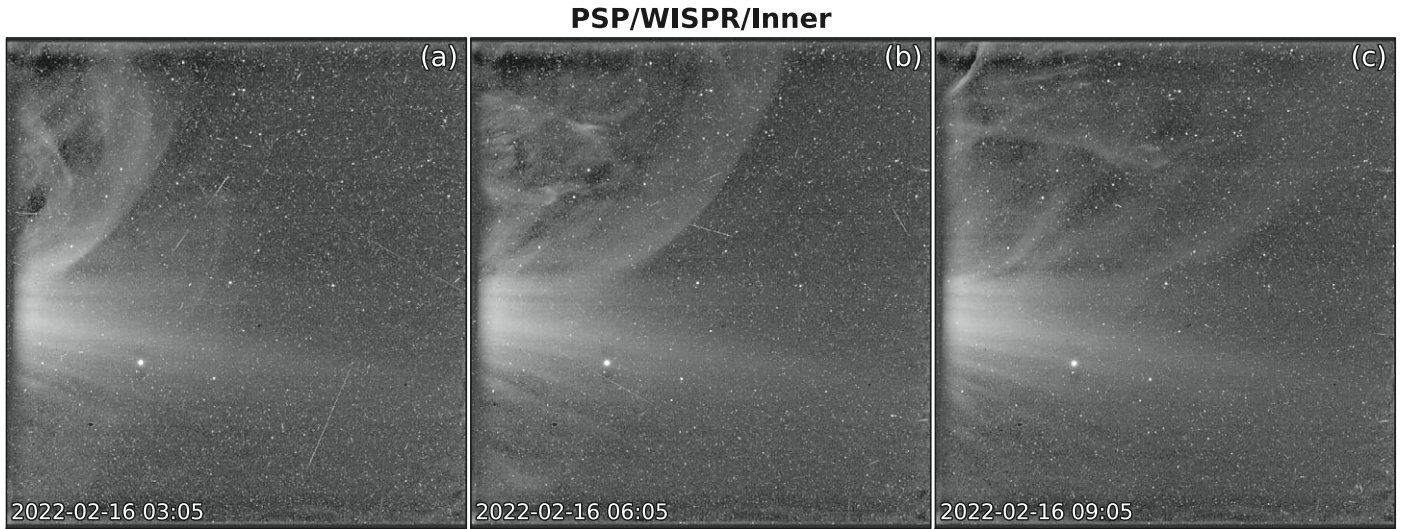
PSP/WISPR/Inner

Figure 12. Overview of the observations of the 2022 February 15 event taken by the WISPR Inner camera on board Parker. The CME is shown as it propagates in three frames separated by 3 hr each. The planet (brightest point) in the lower left quadrant of each image is Earth.

A few images from the WISPR Inner camera containing the 2022 February 15 CME in its field of view are shown in Figure 12. These data were processed via the L3 algorithm developed by the WISPR instrument team and described in Liewer et al. (2023). During our period of interest (2022 February 15–17, i.e., approximately 10 days before the E11 perihelion), WISPR was pointing over the western limb of the Sun (from Parker's viewpoint), as can be seen by the streamer emanating from the left of each frame in Figure 12. The CME was observed to cross the telescope's field of view from left to right predominantly over its top half, indicating that Parker observed a CME that propagated mostly toward the north and experienced little-to-no deflection toward the equatorial plane after leaving the Sun, confirming the assessment in Section 2 based on other available remote-sensing imagery.

As mentioned in Section 4.1, the CME-driven shock impacted Parker on February 16 at 07:25 UT, i.e., between the observation times of panels (b) and (c) of Figure 12. This means that the spacecraft imaged the CME as it was being impacted by it, an occurrence historically considered exceptional and that is becoming more common during the Parker era (e.g., Romeo et al. 2023; Wood et al. 2023) as the probe approaches the Sun by lowering its perihelion and the Solar Cycle 25 activity levels increase. Shortly after the time of the ejecta leading edge passage, i.e., February 16 at 15:18 UT, trailing flows from the CME were observed in the WISPR Outer camera—these images, however, are characterized by high noise levels, and moving features in them can be better appreciated in video format[22]; hence, they are not shown here.

Appendix B
Processing and Calibration of the Bepi Magnetic Field Data

The primary objective of the magnetometer instrument MPO-MAG on board the MPO of the Bepi mission is to map Mercury's magnetic field as well as the interaction of the Hermean magnetosphere with the solar wind. In order to characterize the solar wind at short distances from the Sun (i.e., at Mercury's orbit), MPO-MAG has been in operation during

most of the Bepi cruise phase to Mercury, contributing to studies of solar wind turbulence and transient phenomena (Heyner et al. 2021).

After launch, MPO-MAG was in continuous operation outside the SEPS (Montagnon et al. 2021) periods, until the beginning of 2022, when it was decided that the instrument will remain in operation during these periods in background mode. MPO-MAG observations during arcs remain of high accuracy, but special preprocessing cleaning by the instrument team is needed as the two sensors of the instrument are influenced by the magnetic disturbance field of the spacecraft. The 2022 February 15 event occurred during one of these SEPS arcs, starting on 2022 February 15 at 02:17:20 UT. The main consequences depend on the individual thrusters being used and the thrust levels, and a shift of the components by 10 nT was found, as well as an increase in the noise floor. In this regard, the MPO-MAG team cleaned the data phases and removed the noise for this study by low-pass filtering the field as well as linearly interpolating the time-dependent instrument offsets before and after the event studied in this work. The quality criterion adopted here is the sensor component differences, which should be zero in the case of well-cleaned data.

We consider that the version of the data used in this study is the most accurate available for this event, and the total field and components can be trusted within an error of 10 nT in magnitude. We also note that the arrival times of the shock and sheath match very well with the Bepi high-energy particles observed by the BepiColombo Environment Radiation Monitor (Pinto et al. 2022), the only other instrument in operation during this SEPS arc (these measurements, not shown here, are presented in detail by Khoo et al. 2024). Therefore, we also trust that the timing of the crossing of the different regions of the CME observed by MPO-MAG are accurate.

Appendix C
Flux Rope Fits for the Magnetic Obstacle Interval at Parker

To compare the flux rope fitting results at Bepi with both ejecta interval possibilities at Parker, we repeat the reconstructions shown in Figure 9(b) for the magnetic cloud interval by

---

[22] WISPR movies for the Inner and Outer cameras, sorted chronologically by solar encounter number, are available at https://wispr.nrl.navy.mil/wisprdata.
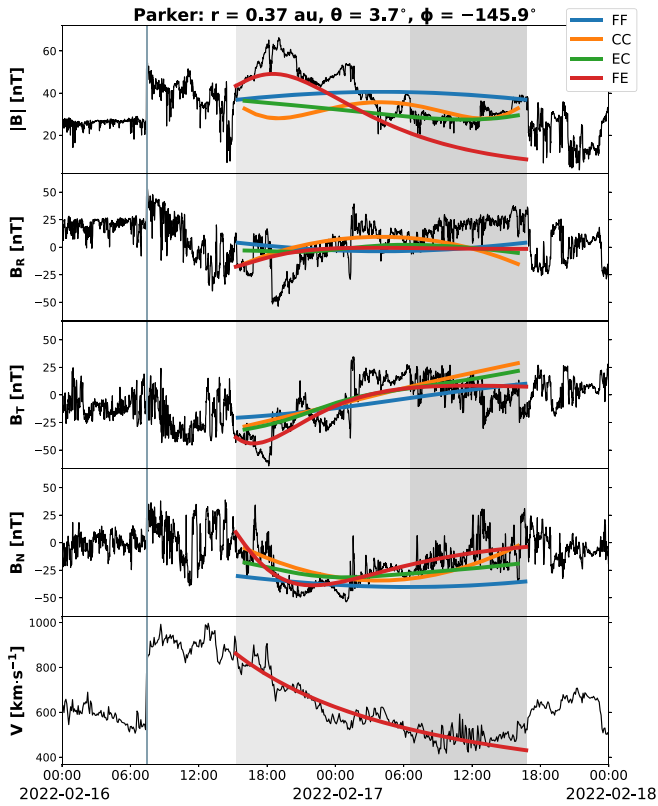
Figure 13. Flux rope fitting results at Parker obtained when considering the full magnetic ejecta interval, showing magnetic field and bulk speed data as well as the corresponding quantities resulting from different flux rope models.

Table 5
Flux Rope Fitting Results for the Full Ejecta Interval at Parker

Flux Rope Parameter	FF	CC	EC	FE
H	$+1$	$+1$	$+1$	$+1$
ϑ_0 [deg]	-7.1	-49.8	-51.4	-59.7
φ_0 [deg]	181.2	1.0	326.5	312.6
B_0 [nT]	71.0	41.6	28.2	83.7
R_0 [au]	0.053	0.135	0.224	0.120
p_0 [R_0^{-1}]	0.905	0.485	0.307	0.430
τ [au^{-1}]	16.32	0.84	1.79	7.21
Φ_{ax} [10^{21} Mx]	0.60	2.92	2.21	3.68
Φ_{po} [10^{21} Mx au^{-1}]	3.50	4.43	5.72	9.37
C1	$\cdots$	1.30	0.65	$\cdots$
ψ [deg]	$\cdots$	$\cdots$	122.8	$\cdots$
δ	$\cdots$	$\cdots$	0.41	$\cdots$

Note. The parameters shown are in the same format as in Table 4. The assumed average speed for the CME ejecta in the FF, CC, and EC fits is 589 km s^{-1}, while the FE procedure uses the time-dependent speed shown in the bottom panel of Figure 13.

retrieves a flux rope structure that is fundamentally different from the corresponding results obtained from the magnetic cloud time series, showcasing the complexity of the structure under analysis.

considering the full magnetic obstacle identified at Parker. These results are presented in Figure 13 and Table 5. As in Figure 9(b), we adopt here all four models considered for the magnetic cloud interval at Parker, i.e., FF, CC, EC, and FE. For the first three fitting procedures, we employ an average solar wind speed of 589 km s^{-1}, while for the FE technique, we use the fitted speed profile shown in the bottom panel of Figure 13, obtained via a second-order polynomial fit to the corresponding Parker data.

In the case of the magnetic obstacle interval at Parker, the different flux rope fitting techniques appear visually significantly less consistent with each other than the ones shown in Figure 9 for both the ejecta at Bepi and the magnetic cloud at Parker. This may be due to the strong asymmetry seen in the magnetic field magnitude between the leading and trailing portions of the magnetic obstacle. The inconsistencies are also reflected in the resulting parameters presented in Table 5, which include, e.g., flux rope axis directions that differ by up to $\sim53°$ in latitude and $\sim180°$ in longitude, as well as impact parameters that range between $\sim30\%$ and $\sim90\%$ away from the central axis along the cross-sectional radius.

Visually, the FE fit appears to better match the data, which is not surprising since this model takes CME expansion into account and the 2022 February 15 event was strongly expanding when it was measured in situ by Parker (as shown in the bottom panel of Figure 13). However, even the FE results do not reproduce the B_R profile particularly well, which on the other hand is poorly fitted by all models even when considering the magnetic cloud interval only (see Figure 9(b)). Overall, each technique applied to the full magnetic obstacle at Parker

ORCID iDs

Erika Palmerio ⓘ https://orcid.org/0000-0001-6590-3479
Fernando Carcaboso ⓘ https://orcid.org/0000-0003-1758-6194
Leng Ying Khoo ⓘ https://orcid.org/0000-0003-0412-1064
Tarik M. Salman ⓘ https://orcid.org/0000-0001-6813-5671
Beatriz Sánchez-Cano ⓘ https://orcid.org/0000-0003-0277-3253
Benjamin J. Lynch ⓘ https://orcid.org/0000-0001-6886-855X
Yeimy J. Rivera ⓘ https://orcid.org/0000-0002-8748-2123
Sanchita Pal ⓘ https://orcid.org/0000-0002-6302-438X
Teresa Nieves-Chinchilla ⓘ https://orcid.org/0000-0003-0565-4890
Andreas J. Weiss ⓘ https://orcid.org/0000-0002-6273-4320
David Lario ⓘ https://orcid.org/0000-0002-3176-8704
Johannes Z. D. Mieth ⓘ https://orcid.org/0000-0002-7539-0803
Daniel Heyner ⓘ https://orcid.org/0000-0001-7894-8246
Michael L. Stevens ⓘ https://orcid.org/0000-0002-7728-0085
Orlando M. Romeo ⓘ https://orcid.org/0000-0002-4559-2199
Andrei N. Zhukov ⓘ https://orcid.org/0000-0002-2542-9810
Luciano Rodriguez ⓘ https://orcid.org/0000-0002-6097-374X
Christina O. Lee ⓘ https://orcid.org/0000-0002-1604-3326
Christina M. S. Cohen ⓘ https://orcid.org/0000-0002-0978-8127
Laura Rodríguez-García ⓘ https://orcid.org/0000-0003-2361-5510
Phyllis L. Whittlesey ⓘ https://orcid.org/0000-0002-7287-5098
Nina Dresing ⓘ https://orcid.org/0000-0003-3903-4649
Philipp Oleynik ⓘ https://orcid.org/0000-0003-0794-7742
Immanuel C. Jebaraj ⓘ https://orcid.org/0000-0002-0606-7172
David Fischer ⓘ https://orcid.org/0000-0002-8435-7220
Daniel Schmid ⓘ https://orcid.org/0000-0001-7818-4338
Ingo Richter ⓘ https://orcid.org/0000-0002-5324-4039

Hans-Ulrich Auster ⬤ https://orcid.org/0000-0003-1411-217X
Federico Fraschetti ⬤ https://orcid.org/0000-0002-5456-4771
Marilena Mierla ⬤ https://orcid.org/0000-0003-4105-7364

References

Abraham-Shrauner, B., & Yun, S. H. 1976, JGR, 81, 2097
Ala-Lahti, M., Ruohotie, J., Good, S., Kilpua, E. K. J., & Lugaz, N. 2020, JGRA, 125, e2020JA028002
Al-Haddad, N., Nieves-Chinchilla, T., Savani, N. P., Lugaz, N., & Roussev, I. I. 2018, SoPh, 293, 73
Al-Haddad, N., Nieves-Chinchilla, T., Savani, N. P., et al. 2013, SoPh, 284, 129
Allen, R. C., Smith, E. J., Anderson, B. J., et al. 2022, FrASS, 9, 1002273
Astropy Collaboration, Price-Whelan, A. M., Lim, P. L., et al. 2022, ApJ, 935, 167
Asvestari, E., Pomoell, J., Kilpua, E., et al. 2021, A&A, 652, A27
Bale, S. D., Goetz, K., Harvey, P. R., et al. 2016, SSRv, 204, 49
Balogh, A., Gonzalez-Esparza, J. A., Forsyth, R. J., et al. 1995, SSRv, 72, 171
Barnard, L. A., de Koning, C. A., Scott, C. J., et al. 2017, SpWea, 15, 782
Benkhoff, J., Murakami, G., Baumjohann, W., et al. 2021, SSRv, 217, 90
Borrini, G., Gosling, J. T., Bame, S. J., & Feldman, W. C. 1982, JGR, 87, 7370
Borrini, G., Gosling, J. T., Bame, S. J., Feldman, W. C., & Wilcox, J. M. 1981, JGR, 86, 4565
Bothmer, V., & Schwenn, R. 1998, AnGeo, 16, 1
Braga, C. R., Vourlidas, A., Liewer, P. C., et al. 2022, ApJ, 938, 13
Brueckner, G. E., Howard, R. A., Koomen, M. J., et al. 1995, SoPh, 162, 357
Burlaga, L., Sittler, E., Mariani, F., & Schwenn, R. 1981, JGR, 86, 6673
Burton, M. E., Smith, E. J., Balogh, A., et al. 1996, A&A, 316, 313
Cane, H. V. 1988, JGR, 93, 1
Carcaboso, F., Gómez-Herrero, R., Espinosa Lara, F., et al. 2020, A&A, 635, A79
Case, A. W., Kasper, J. C., Stevens, M. L., et al. 2020, ApJS, 246, 43
Cécere, M., Sieyra, M. V., Cremades, H., et al. 2020, AdSpR, 65, 1654
Colburn, D. S., & Sonett, C. P. 1966, SSRv, 5, 439
Crooker, N. U., Huang, C. L., Lamassa, S. M., et al. 2004, JGR, 109, A03107
Darnel, J. M., Seaton, D. B., Bethge, C., et al. 2022, SpWea, 20, e2022SW003044
Das, I., Opher, M., Evans, R., Loesch, C., & Gombosi, T. I. 2011, ApJ, 729, 112
Dasso, S., Mandrini, C. H., Luoni, M. L., et al. 2005, in Solar Wind 11/SOHO 16, Connecting Sun and Heliosphere, ed. B. Fleck, T. H. Zurbuchen, & H. Lacoste (Noordwijk: ESA Publications Division), 605
Dasso, S., Nakwacki, M. S., Démoulin, P., & Mandrini, C. H. 2007, SoPh, 244, 115
Davies, E. E., Möstl, C., Owens, M. J., et al. 2021, A&A, 656, A2
Davies, E. E., Winslow, R. M., Scolini, C., et al. 2022, ApJ, 933, 127
DeForest, C., Viall-Kepko, N., Fan, Y., Gibson, S., & Seaton, D. 2023, BAAS, 55, 089
Démoulin, P., Nakwacki, M. S., Dasso, S., & Mandrini, C. H. 2008, SoPh, 250, 347
Domingo, V., Fleck, B., & Poland, A. I. 1995, SoPh, 162, 1
Farrugia, C. J., Berdichevsky, D. B., Möstl, C., et al. 2011, JASTP, 73, 1254
Farrugia, C. J., Erkaev, N. V., Taubenschuss, U., et al. 2008, JGR, 113, A00B01
Farrugia, C. J., Janoo, L. A., Torbert, R. B., et al. 1999, in AIP Conf. Ser. 471, Solar Wind Nine, ed. S. R. Habbal et al. (Melville, NY: AIP), 745
Fox, N. J., Velli, M. C., Bale, S. D., et al. 2016, SSRv, 204, 7
Freeland, S. L., & Handy, B. N. 1998, SoPh, 182, 497
Giacalone, J., Cohen, C. M. S., McComas, D. J., et al. 2023, ApJ, 958, 144
Gibson, S. E., Vourlidas, A., Hassler, D. M., et al. 2018, FrASS, 5, 32
Good, S. W., Ala-Lahti, M., Palmerio, E., Kilpua, E. K. J., & Osmane, A. 2020, ApJ, 893, 110
Good, S. W., Kilpua, E. K. J., LaMoury, A. T., et al. 2019, JGRA, 124, 4960
Gopalswamy, N., Mäkelä, P., Xie, H., Akiyama, S., & Yashiro, S. 2009, JGR, 114, A00A22
Gosling, J. T., Baker, D. N., Bame, S. J., et al. 1987, JGR, 92, 8519
Gui, B., Shen, C., Wang, Y., et al. 2011, SoPh, 271, 111
Guo, F., Giacalone, J., & Zhao, L. 2021, FrASS, 8, 27
Heinemann, S. G., Temmer, M., Farrugia, C. J., et al. 2019, SoPh, 294, 121
Heyner, D., Auster, H. U., Fornaçon, K. H., et al. 2021, SSRv, 217, 52
Howard, R., Liewer, P., & Vourlidas, A. 2023, BAAS, 55, 174
Howard, R. A., Moses, J. D., Vourlidas, A., et al. 2008, SSRv, 136, 67
Illing, R. M. E., & Hundhausen, A. J. 1985, JGR, 90, 275

Isavnin, A., Vourlidas, A., & Kilpua, E. K. J. 2013, SoPh, 284, 203
Janvier, M., Démoulin, P., & Dasso, S. 2014, A&A, 565, A99
Janvier, M., Winslow, R. M., Good, S., et al. 2019, JGRA, 124, 812
Jian, L. K., Russell, C. T., Luhmann, J. G., & Galvin, A. B. 2018, ApJ, 855, 114
Jones, G. H., & Balogh, A. 2000, JGR, 105, 12713
Jones, G. H., Rees, A., Balogh, A., & Forsyth, R. J. 2002, GeoRL, 29, 1520
Kaiser, M. L., Kucera, T. A., Davila, J. M., et al. 2008, SSRv, 136, 5
Kajdič, P., Preisser, L., Blanco-Cano, X., Burgess, D., & Trotta, D. 2019, ApJL, 874, L13
Kallenrode, M. B., Wibberenz, G., Kunow, H., et al. 1993, SoPh, 147, 377
Kasper, J. C., Abiad, R., Austin, G., et al. 2016, SSRv, 204, 131
Kataoka, R., Watari, S., Shimada, N., Shimazu, H., & Marubashi, K. 2005, GeoRL, 32, L12103
Kay, C., Nieves-Chinchilla, T., & Jian, L. K. 2020, JGRA, 125, e2019JA027423
Kay, C., Opher, M., & Evans, R. M. 2015, ApJ, 805, 168
Kay, C., & Palmerio, E. 2024, SpWea, 22, e2023SW003796
Khoo, L. Y., Sánchez-Cano, B., Lee, C. O., et al. 2024, ApJ, 963, 107
Killen, R. M., Sarantos, M., & Reiff, P. H. 2004, AdSpR, 33, 1899
Kilpua, E., Koskinen, H. E. J., & Pulkkinen, T. I. 2017, LRSP, 14, 5
Kilpua, E. K. J., Fontaine, D., Good, S. W., et al. 2020, AnGeo, 38, 999
Kilpua, E. K. J., Fontaine, D., Moissard, C., et al. 2019a, SpWea, 17, 1257
Kilpua, E. K. J., Good, S. W., Dresing, N., et al. 2021, A&A, 656, A8
Kilpua, E. K. J., Good, S. W., Palmerio, E., et al. 2019b, FrASS, 6, 50
Kilpua, E. K. J., Isavnin, A., Vourlidas, A., Koskinen, H. E. J., & Rodriguez, L. 2013, AnGeo, 31, 1251
Kilpua, E. K. J., Liewer, P. C., Farrugia, C., et al. 2009, SoPh, 254, 325
Kilpua, E. K. J., Lumme, E., Andreeova, K., Isavnin, A., & Koskinen, H. E. J. 2015, JGRA, 120, 4112
Kouloumvakos, A., Kwon, R. Y., Rodríguez-García, L., et al. 2022, A&A, 660, A84
Koval, A., & Szabo, A. 2010, JGR, 115, A12105
Lai, H. R., Russell, C. T., Jian, L. K., et al. 2012, SoPh, 278, 421
Lavraud, B., Fargette, N., Réville, V., et al. 2020, ApJL, 894, L19
Lavraud, B., Kieokaew, R., Fargette, N., et al. 2021, A&A, 656, A37
Lavraud, B., Ruffenach, A., Rouillard, A. P., et al. 2014, JGRA, 119, 26
Lepping, R. P., & Behannon, K. W. 1980, JGR, 85, 4695
Lepping, R. P., Jones, J. A., & Burlaga, L. F. 1990, JGR, 95, 11957
Lepri, S. T., & Rivera, Y. J. 2021, ApJ, 912, 51
Li, Y., Luhmann, J. G., & Lynch, B. J. 2018, SoPh, 293, 135
Liewer, P., Panasenco, O., Vourlidas, A., & Colaninno, R. 2015, SoPh, 290, 3343
Liewer, P. C., Vourlidas, A., Stenborg, G., et al. 2023, ApJ, 948, 24
Liu, Y. A., Liu, Y. D., Hu, H., Wang, R., & Zhao, X. 2018, ApJ, 854, 126
Livi, R., Larson, D. E., Kasper, J. C., et al. 2022, ApJ, 938, 138
Lugaz, N., & Farrugia, C. J. 2014, GeoRL, 41, 769
Lugaz, N., Farrugia, C. J., Davies, J. A., et al. 2012, ApJ, 759, 68
Lugaz, N., Farrugia, C. J., Winslow, R. M., et al. 2018, ApJL, 864, L7
Lugaz, N., Lee, C. O., Jian, L. K., et al. 2023, BAAS, 55, 249
Lugaz, N., Salman, T. M., Winslow, R. M., et al. 2020, ApJ, 899, 119
Lugaz, N., Salman, T. M., Zhuang, B., et al. 2022, ApJ, 929, 149
Luhmann, J. G. 1995, AdSpR, 15, 355
Lynch, B. J., Al-Haddad, N., Yu, W., Palmerio, E., & Lugaz, N. 2022, AdSpR, 70, 1614
Maharana, A., Scolini, C., Schmieder, B., & Poedts, S. 2023, A&A, 675, A136
Marubashi, K., & Lepping, R. P. 2007, AnGeo, 25, 2453
Masías-Meza, J. J., Dasso, S., Démoulin, P., Rodriguez, L., & Janvier, M. 2016, A&A, 592, A118
Maunder, M. L., Foullon, C., Forsyth, R., Barnes, D., & Davies, J. 2022, SoPh, 297, 148
Mierla, M., Zhukov, A. N., Berghmans, D., et al. 2022, A&A, 662, L5
Mililio, A., Fujimoto, M., Murakami, G., et al. 2020, SSRv, 216, 93
Moissard, C., Fontaine, D., & Savoini, P. 2019, JGRA, 124, 8208
Montagnon, E., Budnik, F., Casale, M., et al. 2021, SSRv, 217, 32
Möstl, C., Farrugia, C. J., Kilpua, E. K. J., et al. 2012, ApJ, 758, 10
Möstl, C., Rollett, T., Frahm, R. A., et al. 2015, NatCo, 6, 7135
Möstl, C., Weiss, A. J., Reiss, M. A., et al. 2022, ApJL, 924, L6
Müller, D., St. Cyr, O. C., Zouganelis, I., et al. 2020, A&A, 642, A1
Nakagawa, T., Nishida, A., & Saito, T. 1989, JGR, 94, 11761
Neugebauer, M. 2013, SSRv, 176, 125
Neugebauer, M., Clay, D. R., & Gosling, J. T. 1993, JGR, 98, 9383
Nieves-Chinchilla, T., Alzate, N., Cremades, H., et al. 2022, ApJ, 930, 88
Nieves-Chinchilla, T., Jian, L. K., Balmaceda, L., et al. 2019, SoPh, 294, 89
Nieves-Chinchilla, T., Linton, M. G., Hidalgo, M. A., & Vourlidas, A. 2018a, ApJ, 861, 139

Nieves-Chinchilla, T., Linton, M. G., Hidalgo, M. A., et al. 2016, ApJ, 823, 27
Nieves-Chinchilla, T., Vourlidas, A., Raymond, J. C., et al. 2018b, SoPh, 293, 25
Nykyri, K., Ma, X., Burkholder, B., et al. 2023, FrASS, 10, 1179344
Oh, S. Y., Yi, Y., & Kim, Y. H. 2007, SoPh, 245, 391
Owens, M. J., Cargill, P. J., Pagel, C., Siscoe, G. L., & Crooker, N. U. 2005, JGR, 110, A01105
Owens, M. J., Lockwood, M., & Barnard, L. A. 2017, NatSR, 7, 4152
Pal, S., Balmaceda, L., Weiss, A. J., et al. 2023, FrASS, 10, 1195805
Pal, S., Kilpua, E., Good, S., Pomoell, J., & Price, D. J. 2021, A&A, 650, A176
Pal, S., Lynch, B. J., Good, S. W., et al. 2022, FrASS, 9, 903676
Palmerio, E., Kilpua, E. K. J., Möstl, C., et al. 2018, SpWea, 16, 442
Palmerio, E., Kilpua, E. K. J., & Savani, N. P. 2016, AnGeo, 34, 313
Palmerio, E., Lee, C. O., Mays, M. L., et al. 2022a, SpWea, 20, e2021SW002993
Palmerio, E., Lee, C. O., Richardson, I. G., et al. 2022b, SpWea, 20, e2022SW003215
Palmerio, E., Lynch, B. J., Lee, C. O., et al. 2023a, BAAS, 55, 307
Palmerio, E., Maharana, A., Lynch, B. J., et al. 2023b, ApJ, 958, 91
Palmerio, E., Nieves-Chinchilla, T., Kilpua, E. K. J., et al. 2021, JGRA, 126, e2021JA029770
Pérez-Alanis, C. A., Janvier, M., Nieves-Chinchilla, T., et al. 2023, SoPh, 298, 60
Pinto, M., Sanchez-Cano, B., Moissl, R., et al. 2022, SSRv, 218, 54
Regnault, F., Al-Haddad, N., Lugaz, N., et al. 2024, ApJ, 962, 190
Regnault, F., Janvier, M., Démoulin, P., et al. 2020, JGRA, 125, e2020JA028150
Richardson, I. G., & Cane, H. V. 2004, JGR, 109, A09104
Richardson, I. G., & Cane, H. V. 2010, SoPh, 264, 189
Richter, A. K., Hsieh, K. C., Luttrell, A. H., Marsch, E., & Schwenn, R. 1985, GMS, 35, 33
Riley, P., Linker, J. A., Lionello, R., et al. 2004, JASTP, 66, 1321
Rivera, Y. J., Raymond, J. C., Landi, E., et al. 2022, ApJ, 936, 83
Rivera, Y. J., Raymond, J. C., Reeves, K. K., et al. 2023, ApJ, 955, 65
Rochus, P., Auchère, F., Berghmans, D., et al. 2020, A&A, 642, A8
Rodriguez, L., Masías-Meza, J. J., Dasso, S., et al. 2016, SoPh, 291, 2145
Rodriguez, L., Zhukov, A. N., Dasso, S., et al. 2008, AnGeo, 26, 213
Rodríguez-García, L., Nieves-Chinchilla, T., Gómez-Herrero, R., et al. 2022, A&A, 662, A45
Romeo, O. M., Braga, C. R., Badman, S. T., et al. 2023, ApJ, 954, 168
Ruan, M., Zuo, P., Feng, X., et al. 2023, ApJ, 951, 47
Ruffenach, A., Lavraud, B., Farrugia, C. J., et al. 2015, JGRA, 120, 43
Ruffenach, A., Lavraud, B., Owens, M. J., et al. 2012, JGR, 117, A09101
Russell, C. T., Mellott, M. M., Smith, E. J., & King, J. H. 1983, JGR, 88, 4739
Salman, T. M., Lugaz, N., Winslow, R. M., et al. 2021, ApJ, 921, 57
Salman, T. M., Winslow, R. M., & Lugaz, N. 2020, JGRA, 125, e2019JA027084
Savani, N. P., Owens, M. J., Rouillard, A. P., Forsyth, R. J., & Davies, J. A. 2010, ApJL, 714, L128
Savani, N. P., Owens, M. J., Rouillard, A. P., et al. 2011, ApJ, 732, 117
Schwartz, S. J. 1998, ISSIR, 1, 249
Scolini, C., Chané, E., Temmer, M., et al. 2020, ApJS, 247, 21
Scolini, C., Dasso, S., Rodriguez, L., Zhukov, A. N., & Poedts, S. 2021, A&A, 649, A69
Scolini, C., Rodriguez, L., Mierla, M., Pomoell, J., & Poedts, S. 2019, A&A, 626, A122
Siscoe, G., & Odstrcil, D. 2008, JGR, 113, A00B07
Sonnerup, B. U. O., & Cahill, L. J. J. 1967, JGR, 72, 171
SunPy Community, Barnes, W. T., Bobra, M. G., et al. 2020, ApJ, 890, 68
Temmer, M., & Bothmer, V. 2022, A&A, 665, A70
Temmer, M., Veronig, A. M., Peinhart, V., & Vršnak, B. 2014, ApJ, 785, 85
Thernisien, A. 2011, ApJS, 194, 33
Thompson, W. T., Kliem, B., & Török, T. 2012, SoPh, 276, 241
Trotta, D., Vuorinen, L., Hietala, H., et al. 2022, FrASS, 9, 1005672
Verbeke, C., Mays, M. L., Kay, C., et al. 2023, AdSpR, 72, 5243
Viall, N. M., DeForest, C. E., & Kepko, L. 2021, FrASS, 8, 139
Viñas, A. F., & Scudder, J. D. 1986, JGR, 91, 39
Volkmer, P. M., & Neubauer, F. M. 1985, AnGeo, 3, 1
Vourlidas, A., Colaninno, R., Nieves-Chinchilla, T., & Stenborg, G. 2011, ApJL, 733, L23
Vourlidas, A., Howard, R. A., Plunkett, S. P., et al. 2016, SSRv, 204, 83
Vourlidas, A., Lynch, B. J., Howard, R. A., & Li, Y. 2013, SoPh, 284, 179
Vourlidas, A., Wu, S. T., Wang, A. H., Subramanian, P., & Howard, R. A. 2003, ApJ, 598, 1392
Vršnak, B., Amerstorfer, T., Dumbović, M., et al. 2019, ApJ, 877, 77
Wang, C., Du, D., & Richardson, J. D. 2005, JGR, 110, A10107
Wang, Y., Shen, C., Wang, S., & Ye, P. 2004, SoPh, 222, 329
Whittlesey, P. L., Larson, D. E., Kasper, J. C., et al. 2020, ApJS, 246, 74
Winslow, R. M., Lugaz, N., Philpott, L. C., et al. 2015, JGRA, 120, 6101
Winslow, R. M., Philpott, L., Paty, C. S., et al. 2017, JGRA, 122, 4960
Winslow, R. M., Scolini, C., Lugaz, N., & Galvin, A. B. 2021, ApJ, 916, 40
Witasse, O., Sánchez-Cano, B., Mays, M. L., et al. 2017, JGRA, 122, 7865
Woo, R., Armstrong, J. W., Sheeley, N. R., et al. 1985, JGR, 90, 154
Wood, B. E., Hess, P., Chen, Y., & Hu, Q. 2023, ApJ, 953, 123
Yurchyshyn, V., Hu, Q., Lepping, R. P., Lynch, B. J., & Krall, J. 2007, AdSpR, 40, 1821
Zhuang, B., Lugaz, N., Al-Haddad, N., et al. 2023, ApJ, 952, 7
Zurbuchen, T. H., & Richardson, I. G. 2006, SSRv, 123, 31
Zurbuchen, T. H., Weberg, M., von Steiger, R., et al. 2016, ApJ, 826, 10